Early Mesozoic Anatexis-Induced Strain Partitioning and Gneiss Doming in the Yunkai Massif, South China: A Response to Contrasted Dynamics of Paleo-Pacific and Paleo-Tethys Subductions?

Bryan Cochelin, Bo Wang, Jiashuo Liu, Shenghua Lu, Liangshu Shu, Charles Gumiaux, Yan Chen, Fang Song

Tectonics®

RESEARCH ARTICLE
10.1029/2022TC007457

Key Points:

- The anatectic domains of the Yunkai massif recorded NE-SW regional lateral flow leading to the formation of gneiss domes
- Anatexis-induced strain partitioning led to co-occurrence of lateral horizontal, strike-slip, and vertical flow
- Late Permian-Middle Triassic lateral flow in Yunkai resulted from Paleo-Pacific subduction rather than Indosinian orogeny

Supporting Information:

Supporting Information may be found in the online version of this article.

Correspondence to:

B. Wang,
bwang@nju.edu.cn

Citation:

Cochelin, B., Wang, B., Liu, J., Lu, S., Shu, L., Gumiaux, C., et al. (2022). Early Mesozoic anatexis-induced strain partitioning and gneiss doming in the Yunkai massif, South China: A response to contrasted dynamics of Paleo-Pacific and Paleo-Tethys subductions? *Tectonics*, *41*, e2022TC007457. https://doi.org/10.1029/2022TC007457

Received 13 JUN 2022
Accepted 21 SEP 2022

Author Contributions:

Conceptualization: Bryan Cochelin, Bo Wang, Liangshu Shu, Yan Chen
Formal analysis: Bryan Cochelin, Jiashuo Liu, Shenghua Lu, Fang Song
Funding acquisition: Bryan Cochelin, Bo Wang, Liangshu Shu, Charles Gumiaux, Yan Chen
Investigation: Bryan Cochelin, Bo Wang, Jiashuo Liu, Shenghua Lu, Liangshu Shu, Charles Gumiaux, Fang Song
Project Administration: Bo Wang, Liangshu Shu, Charles Gumiaux, Yan Chen
Resources: Shenghua Lu
Software: Bryan Cochelin, Jiashuo Liu, Shenghua Lu
Supervision: Bryan Cochelin, Bo Wang, Liangshu Shu, Charles Gumiaux, Yan Chen

Early Mesozoic Anatexis-Induced Strain Partitioning and Gneiss Doming in the Yunkai Massif, South China: A Response to Contrasted Dynamics of Paleo-Pacific and Paleo-Tethys Subductions?

Bryan Cochelin[1], Bo Wang[1], Jiashuo Liu[1], Shenghua Lu[1], Liangshu Shu[1], Charles Gumiaux[2], Yan Chen[2], and Fang Song[1]

[1]State Key Laboratory for Mineral Deposits Research, School of Earth Sciences and Engineering, Nanjing University, Nanjing, China, [2]Université d'Orléans, CNRS, BRGM, ISTO, Orléans, France

Abstract This study aims to decipher the structural impact of late anatexis in the core of polycyclic basements, like the Cathaysia Block (South China). Based on field mapping and detailed structural and kinematic analyses in the southern part of the Yunkai massif, we document anatexis-induced strain partitioning and gneiss dome formation. The exhumation of migmatites within gneiss domes occurred in a context of NE-SW regional extension coupled with syn-anatexis (a) horizontal lateral flow and vertical one in their cores, (b) strike-slip dominated flow at the limbs of domes, and (c) constrictive lateral flow at the external parts. Petrographic and microstructural analyses suggest that the cores of the gneiss domes and plutons recorded magmatic to sub-solidus deformation while strain localization at the top of gneiss domes is characterized by retrogressive shearing. Zircons U-Pb dating of diatexites and late-kinematic plutons give coherent crystallization ages of ca. 240 Ma, suggesting that the regional partial melting and gneiss doming occurred in the Triassic and probably as early as Late Permian, rather than during the Early Paleozoic as previously thought. A regional NE-SW lateral flow in the deep crust is fully compatible with NW-SE horizontal shortening, as also exemplified for Late Permian to Middle Triassic times in the whole Cathaysia and the Xuefengshan belt. Therefore, the Yunkai massif should no longer be considered as belonging to the Indosinian belt, instead, orogen-parallel crustal flow in the Yunkai massif looks rather controlled by the subduction of the Paleo-Pacific plate at the eastern margin of the South China Block.

1. Introduction

Deciphering the tectonic evolution of polycyclic orogenic basements is not always straightforward and remains a significant issue for many orogenic belts. It is especially the case in ancient mountain belts that were affected by later polyphasic orogenic deformation, widespread magmatism, and/or strong metamorphic overprint, and where a long-lived erosion reworked most of the stratigraphic markers (e.g., post-orogenic deposits; Cochelin, Lemirre, et al., 2018; da Silva et al., 2016; Nosenzo et al., 2022). Avoiding tectonic and geodynamic misinterpretations when studying these polycyclic basements thus requires careful multi-disciplinary studies coupled with an integrative view of the full tectonic history of these orogenic belts. Such a challenging aspect is particularly exemplified in South China, and especially the south-eastern part of the South China Block (i.e., Cathaysia, Figure 1a) that was affected by three distinct orogenic cycles, at Neoproterozoic, Silurian, and Triassic times (e.g., Shu et al., 2021). While the Neoproterozoic orogeny that forms the Jiangnan belt was restricted to the boundary between the Yangtze and the Cathaysia sub-blocks (Figure 1a), the Early Paleozoic Orogeny (EPO) that developed at Silurian times occupies the whole Cathaysia and is responsible to intense deformation, widespread magmatism and high-temperature (HT) metamorphism (Shu et al., 2015; Figure 1b). The EPO is thus considered as the main orogenic event that affected Cathaysia and structured its basement. During the Permian-Triassic, the subduction of the different branches of the Paleo-Tethys led to the formation of narrow high-pressure orogenic belts at the northern (i.e., the Diabieshan) and south-western (i.e., the Indosinian orogen) margins of the South China Block (Faure et al., 2016; J. Li, Zhang, et al., 2017; Y. J. Wang et al., 2018). Coeval and hypothetical subduction of the Paleo-Pacific plate at the eastern margin of the South China Block has been also proposed and may have induced significant intraplate deformation (e.g., A. Chen et al., 1999; Chu, Faure, et al., 2012; J. Li, Zhang, et al., 2017; J. Li, Zhao, et al., 2017; Z.-X. Li & Li, 2007).

Validation: Bryan Cochelin, Bo Wang, Jiashuo Liu, Liangshu Shu, Charles Gumiaux, Yan Chen
Visualization: Bryan Cochelin, Bo Wang, Shenghua Lu
Writing – original draft: Bryan Cochelin, Bo Wang, Liangshu Shu, Charles Gumiaux, Yan Chen

However, the relative tectonic influence of the Indosinian orogeny and the subduction of the Paleo-Tethys and Paleo-Pacific oceans on the basement inherited from the Silurian times in South China is still widely debated. Late Permian to Middle Triassic intraplate deformation was mainly described as localized within strike-slip corridors or as a fold-and-thrust-belt (i.e., typical of cold lithospheres, A. Chen et al., 1999; Chu, Faure, et al., 2012; J. Li, Zhang, et al., 2017; Xu et al., 2011), but numerous geochronological and petrological studies of the last two decades highlighted that the lower crust experienced partial melting with (a) sparse Permian to Triassic magmatism associated with magmatic arc or collisional environments (Gao et al., 2017 and references therein) coupled with (b) occurrences of HT metamorphism ranging from amphibolite to granulite facies forming gneiss domes within the core of the EPO, like in the Wuyi and the Yunkai massifs (Lin et al., 2008; L. Zhao et al., 2010; L. Zhao, Zhai, Santosh, & Zhou, 2017; D. Z. Wang et al., 2001; Figure 1a). The tectonic origin and the significance of these Late Permian-Triassic high-grade rocks remain yet unconstrained due to the lack of structural data.

This study aims to clarify the tectonic context for the formation of anatectic domes from the previously considered EPO in the Yunkai massif (Figure 1a), where a strong thermal Indosinian event has been proposed by some authors (e.g., C.-H. Chen et al., 2017; X. Wang et al., 2020; Y. J. Wang, Fan, Cawood, et al., 2007; Y. J. Wang et al., 2021) while some others consider that high-grade ductile fabrics and partial melting are inherited from Silurian times (e.g., Z. Chen et al., 2021; Lin et al., 2008; J. Zhang et al., 2019; Zhong et al., 1996). In this paper, we explore how the gneiss domes of the southern parts of South China were generated by providing new precise geological maps and a new structural and kinematic study in the southern part of the Yunkai Massif, as no detailed field mapping of structural studies have yet been carried out in this area. Additional petrographic and microstructural studies coupled with new geochronological constraints for magmatism, metamorphism, and deformation using U-Pb dating on zircons are provided to constrain the tectono-metamorphic evolution of the anatectic complexes. We present that migmatites from the Yunkai Massif were exhumed accommodating orogen-parallel (i.e., NE-SW lateral escape) to slightly oblique extension or vertical flow (i.e., gravity-driven) between the Late Permian and the Middle Triassic in a context of NW-SE convergence, reworking the earlier structures inherited from the Silurian orogeny. The relative influence of the Indosinian orogeny, the subduction of the Paleo-Tethys and Paleo-Pacific oceans is discussed and a new 3D deformation model is proposed to explain the atypical strain pattern from the Yunkai massif. Evidence of large-scale ductile flow within the mid-lower crust place the currently prevailing model of the Early Mesozoic tectonic overprint in South China in a new perspective as the accommodation of shortening was not restricted to the formation of a fold-and-thrust-belt or localized strike-slip corridors.

2. Geological Settings

2.1. The Polycyclic Evolution of South China

The South China Block results from the collision of two principal continental sub-blocks (i.e., Yangtze and Cathaysia) during the Neoproterozoic leading to the formation of the Jiangnan Orogen (e.g., Guo et al., 1989; X.-H. Li et al., 2009; Z. X. Li et al., 2008; Shu et al., 2019; Figure 1a). In the Early Paleozoic (i.e., Late Ordovician to Silurian), the EPO was formed at the expense of the whole Cathaysia Block and the southern border of the Yangtze Block, reworking a part of the Jiangnan Orogen (Figure 1a). The main Early Paleozoic orogenic phase is characterized by the development of the doubly verging orogenic belt, which is centered on Cathaysia (e.g., Charvet et al., 2010; J. Li, Zhao, et al., 2017; Shu et al., 2015; Figure 1b). In its core, deep crustal domains were exhumed within gneiss domes, mainly cropping in the Wuyi and Yunkai massifs (Figures 1a and 1b; Faure et al., 2009; Lin et al., 2008). This lower unit of the EPO is characterized by gneiss and migmatites, resulting from syn-to late-collisional HT metamorphism. The age of the partial melting and amphibolite facies metamorphism is well-constrained, having taken place from 455 to 430 Ma (Shu et al., 2015; B. Wang et al., 2014; D. Wang et al., 2013; J.-Q. Wang et al., 2017). Partial melting in the lower crust is associated with the intrusion of numerous peraluminous S-type plutons in both the lower and upper crusts (Figure 1b) between 455 and 415 Ma (Shu et al., 2021 and reference therein). Deformation within the lower unit is described as strongly heterogeneous, ranging from low strain sub-magmatic to mylonitic fabrics (e.g., Faure et al., 2009). The structures are also variable, with (a) strike-slip or transpressional shear zones crosscutting the lower unit (J. Li, Zhang, et al., 2017; J. Li, Zhao, et al., 2017; Shu et al., 2015) and (b) penetrative flat foliation or domal structures associated with orogen-parallel stretching (Faure et al., 2009).

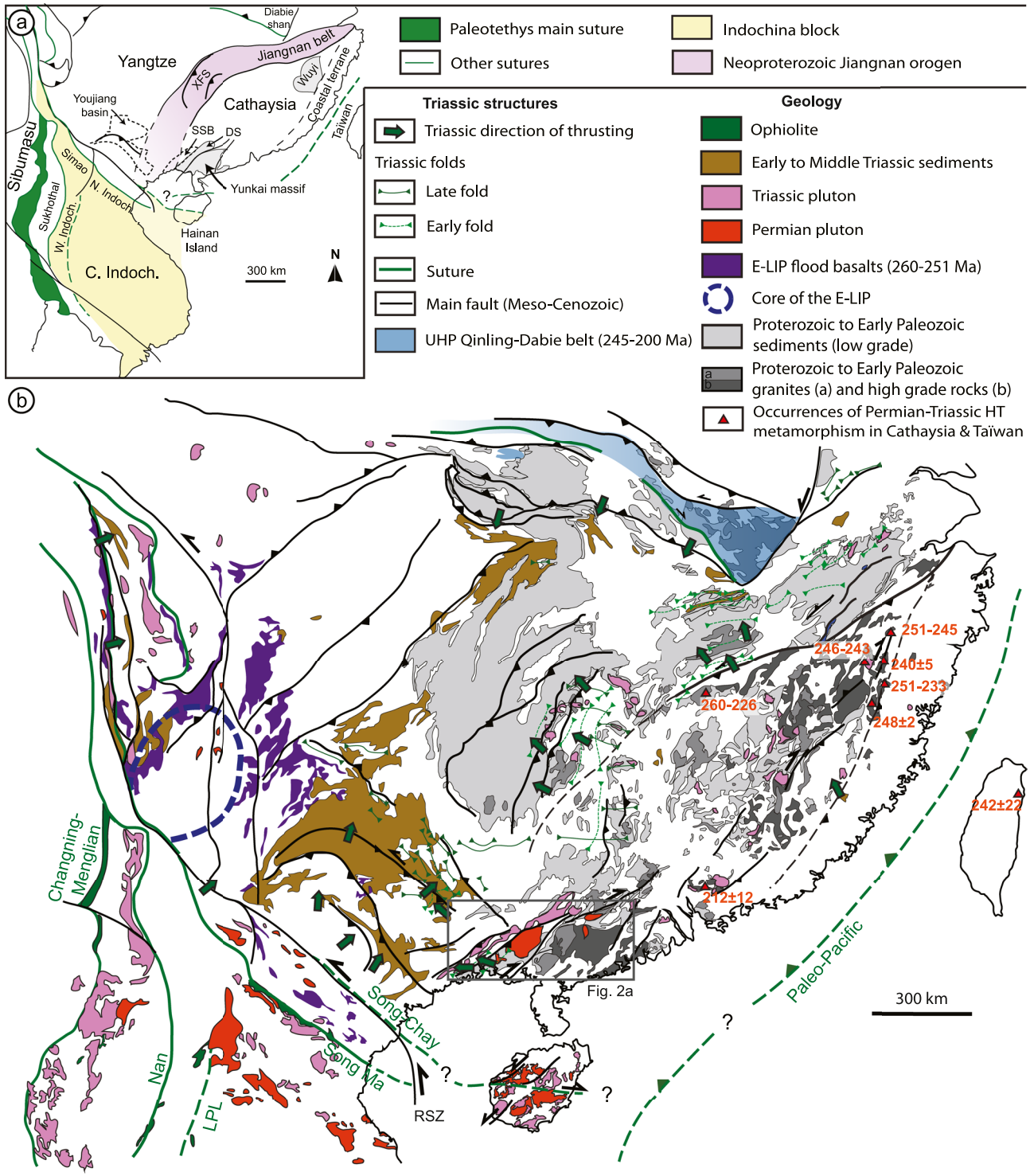

Figure 1. (a) Distribution of the main geological and tectonic features and continental blocks in South East Asia; (b) simplified tectonic and geological map of the South China Block. The main kinematics of thrusts are from Chu and Lin (2014), Chu, Faure, et al. (2012), Faure et al. (2014, 2016), Hacker et al. (2004), J. Li, Zhang, et al. (2017), J. Li, Zhao, et al. (2017), and Lin et al. (2001, 2008). Occurrences of Permian-Triassic HT metamorphism in the Wuyi, Bayun massifs, and Taïwan are from Z.-X. Li and Li (2007), D. Z. Wang et al. (2001), Xiang et al. (2008), L. Zhao, Zhai, et al. (2017), and L. Zhao et al. (2015) and references therein. The occurrences of Permian-Triassic HT metamorphism in the Yunkai massif are only presented in Figure 2a. Abbreviations: DG, Darongshan; LPL, Luang Prabang-Loi suture; SSB, Shiwandashan basin; XFS, Xuefengshan belt; RSZ, Red River Shear Zone.

The South China Block was then heterogeneously reworked during the Late Paleozoic and Mesozoic. The progressive closure of the northern and southern branches of the Paleo-Tethys during the Late Paleozoic led to the formation of the Dabieshan and Indosinian belts at the northern and south-western margin of the South China Block, respectively (e.g., J. Li, Zhang, et al., 2017; Shu et al., 2021; Figures 1a and 1b). Even if the dynamics of the southern branch of the Paleo-Tethys is still debated, the north-eastward subduction of the main Paleo-Tethys Ocean located between the Sibumasu Block and the Sukhothai arc is commonly admitted (see Y. J. Wang et al., 2018 and reference therein, Figure 1a). The accretion of Indochina fragments (i.e., the back-arc realm of the Paleo-Tethys) to the South China Block results in the southward subduction of the Jinshajiang-Ailaoshan-Song Ma branch (JASB) during the Late Permian and Early Triassic, inducing intense arc-related magmatism in North Indochina (e.g., Hieu et al., 2020; Thanh et al., 2019; Y. J. Wang et al., 2018). The following collision, called Indosinian, occurred at ca. 245–230 Ma, with the development and the exhumation of HP rocks coupled with syn-collisional magmatism in the narrow hinterland (Fan et al., 2015; Y. J. Wang et al., 2018; R. Y. Zhang et al., 2013, and references therein) and was followed by the accretion of the Sibumasu Block to the South China-Indochina Block at the Late Triassic-Early Jurassic (i.e., Cimmerian orogeny, Faure et al., 2018). Most of the Paleo-Tethysian ophiolites were formed during the Carboniferous, but MORB were still produced between Indochina and South China until ca. 265 Ma (R. Y. Liu et al., 2018; Y. J. Wang et al., 2018; R. Y. Zhang et al., 2014). Contrary to Indochina, the South China Block formed a large shallow to deep marine domain at Late Paleozoic times (Y. Wang & Jin, 2000). Terrestrial environments were restricted to magmatic provinces, the one forming an NE-SW range at the eastern part of Cathaysia (including the Yunkai massif; Y. Wang & Jin, 2000) and the second centered on the 261–250 Ma Emeishan Large Igneous Province (E-LIP) in the western Yangtze Block (Shellnutt, 2014; X. Wang et al., 2020; Figure 1b). It has been proposed that Late Permian-Early Triassic magmatism along the eastern margin of the South China Block was related to the subduction of the Paleo-Pacific Ocean (Isozaki et al., 2017; Jiao et al., 2015; J. Li, Zhao, et al., 2017; X.-H. Li et al., 2012; Z.-X. Li & Li, 2007; Q. Wang, Li, et al., 2005; X. Zhang et al., 2018). The progressive emersion of the whole South China Block occurred during the Early to Late Triassic (Y. Wang & Jin, 2000) in response to the propagation of the main deformation front and associated intraplate deformation (J. Li, Zhang, et al., 2017; Z.-X. Li & Li, 2007).

In the whole Cathaysia, the deformation was characterized by the formation of a fold-and-thrust-belt that was propagated northwestwards (A. Chen, 1999; Chu & Lin, 2018; Chu, Faure, et al., 2012; Faure et al., 2016; Z.-X. Li & Li, 2007; Y. J. Wang, Li, et al., 2005). It reached the eastern margin of the Yangtze Block and the Neoproterozoic Jiangnan belt (i.e., the Xuefangshan), forming an 800 km wide shortened domain (Figure 1), recently interpreted by Chu et al. (2020) as a probable orogenic plateau. Indeed, intraplate deformation was associated with local HT amphibolite to granulite metamorphism, especially within the Wuyi and Yunkai massifs between ca. 260 and 230 Ma (Z.-X. Li & Li, 2007; D. Z. Wang et al., 2001; Xiang et al., 2008; L. Zhao et al., 2010; L. Zhao, Zhai, et al., 2017; L. Zhao et al., 2015) and scattered syn-to post-kinematic magmatism (e.g., Chu, Lin, et al., 2012; Gao et al., 2017; Song et al., 2017; B. Wang et al., 2014; Figure 1b). Recently, HT horizontal orogen-parallel ductile flow has been described in the Wuyi belt between ca. 245 and 235 Ma (J. Li et al., 2022; X. Zhou et al., 2022). On the contrary, the propagation of the Indosinian deformation front within its northern foreland between 240 and 225 Ma (e.g., the Youjiang basin) is devoid of magmatism or HT metamorphism (W.-X. Yang et al., 2021). In the eastern parts of the Middle Triassic Youjiang basin, north-west verging folds and thrusts were overprinted by Indosinian north-verging structures, suggesting that these two strain patterns were partly diachronous and related to contrasted geodynamic settings (J. Li, Zhao, et al., 2017; Figure 1b). The South China Block was then affected by widespread magmatism both in the Jurassic and the Cretaceous, linked to the ongoing subduction of the Paleo-Pacific Ocean at the east of the Asian plate (Shu et al., 2021 and reference therein).

2.2. Geological Overview of the Yunkai Massif

The Yunkai massif forms the south-westernmost part of the EPO (Figures 1a and 1b). It shows an ENE-WSW trend and is bounded to the west by the Darongshan ranges and the Mesozoic Shiwandashan basin (Figure 1a). The core of the massif is mainly composed of gneiss, migmatites, and granites (Figure 2a) resulting from the Early Paleozoic metamorphic and magmatic event at ca. 455–410 Ma (Figure 2b), unconformably covered by weakly metamorphic Late Paleozoic sedimentary rocks (BGMRGD, 1988; BGMRGX, 1985). The massif was then affected by an intense Permian-Triassic thermal event highlighted by the intrusion of numerous plutons within and around the massif (Figure 2a). These plutons were emplaced between 265 and 235 Ma, with two main peaks, at ca. 260–255 Ma and ca. 245–240 Ma (Figure 2c). The plutons are peraluminous and mostly issued from

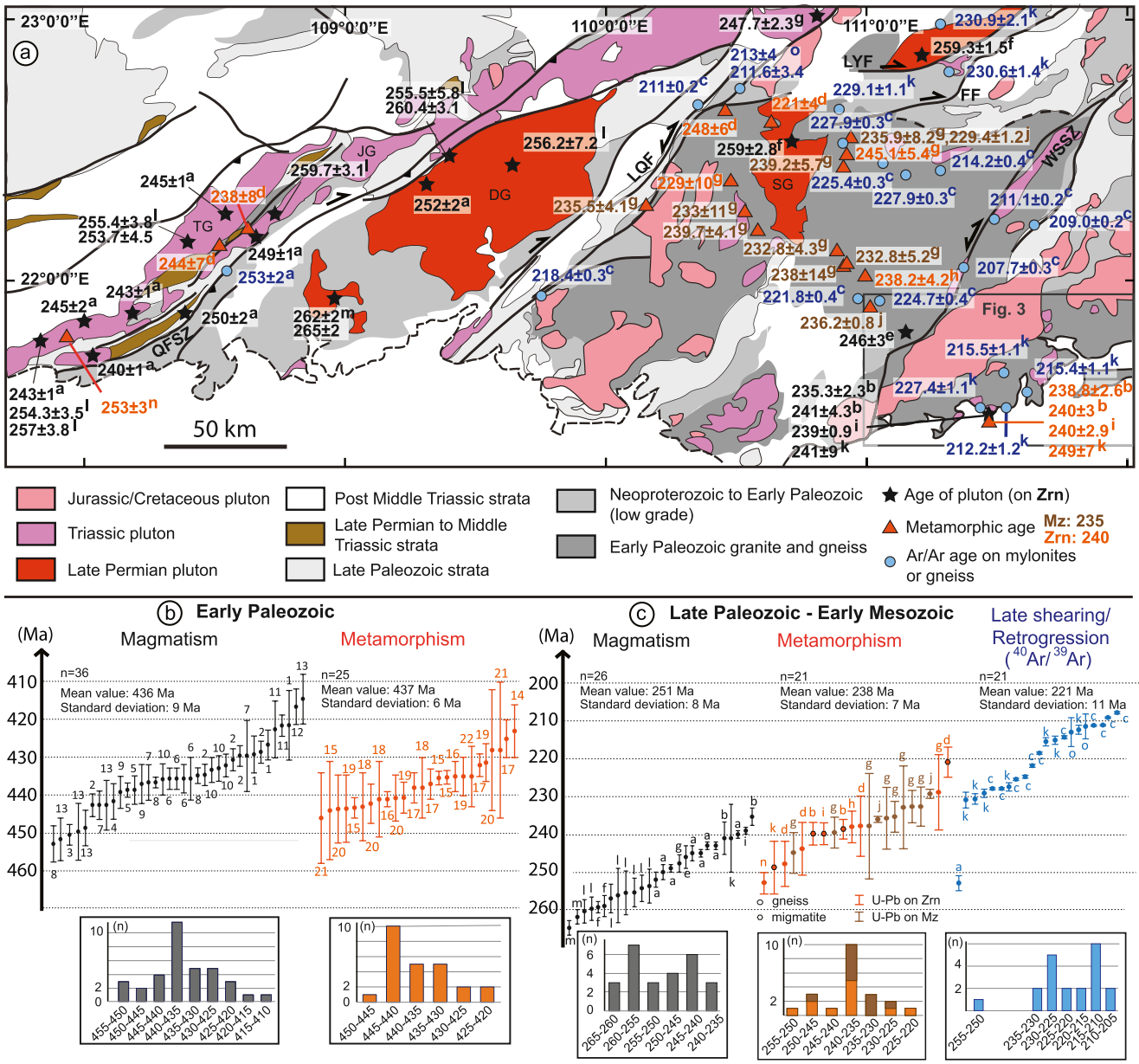

Figure 2. (a) Geological map of the Yunkai massif and surrounding areas, where the available geochronological data used in (c) are located. Abbreviations: QFSZ, Qin-Fang Shear Zone; LQF, Luchuang-Qinxi Fault; LYF, Luoding-Yuecheng Fault; FF, Fenjie Fault; WSSZ, Wuchuang-Sihui Shear Zone; (b) synthesis of available U-Pb ages and associated frequency diagram for Early Paleozoic plutons and metamorphic ages within the Yunkai massif (location not represented in (a)); (c) synthesis of available U-Pb ages and associated frequency diagram for Permian-Triassic plutons, metamorphic and ^{40}Ar/^{39}Ar ages within the Yunkai massif. Each letter and number refer to a specific reference, see Supporting Information S1 for the correspondence.

the partial melting of the crust (Gao et al., 2017; and reference therein) but a hypothetical mantle contribution has been evocated for a few plutons (e.g., Y. Li et al., 2016). Two types of plutons were recognized based on the mineralogical content, (a) the garnet-orthopyroxene granites, which were formed at temperatures comprised between 800°C and 950°C, and (b) the biotite, two micas or cordierite granites that were formed and crystallized at lower temperatures (i.e., <800°C; e.g., Charoy & Barbey, 2008; Jiao et al., 2015; Qing et al., 2020). The first type was mostly recognized at the western boundary of the Yunkai massif (i.e., the Darongshan suite) and few contain granulite xenoliths (Charoy & Barbey, 2008; L. Zhao et al., 2010). A part of these plutons intruded the uppermost parts of the crust (Charoy & Barbey, 2008), reaching the Late Permian-Early Triassic deposits (e.g., the Shiwandashan basin; Figure 2a). All of these plutons were emplaced along regional NE-SW striking faults

and shear zones (Figure 2a). The second type mainly crops within or immediately around the gneissic core of the Yunkai massif, and was emplaced at ca. 10–15 km depth (e.g., Charoy & Barbey, 2008). The HT peak metamorphism that might have induced partial melting in the Darongshan and Shiwandashan areas occurred at ca. 255 Ma, under granulite facies around 0.5–0.6 GPa (Charoy & Barbey, 2008; K. Zhao, Xu, Erdmann, Liu, & Xia, 2017; L. Zhao et al., 2010). The core of the Yunkai massif mostly recorded HT amphibolite facies metamorphism, highlighted by a peak frequency at 240–235 Ma of zircons and monazites ages (Figure 2c) and this metamorphism may have lasted up to ca. 220 Ma. A first peak frequency of $^{40}Ar/^{39}Ar$ ages at ca. 230–225 Ma, obtained on amphibolite facies gneiss, suggests that the massif was then cooled down to 300°C–350°C (Y. J. Wang, Fan, Cawood, et al., 2007; Y. J. Wang et al., 2021), that is, the closure temperature of biotite and muscovite (Dodson, 1973; Harrison et al., 1985).

Lin et al. (2008) highlighted that the Yunkai massif is characterized by shallowly dipping foliation planes forming a ca. 100 × 50 km^2 domal structure, which is cored by anatectic granites and migmatites. They detailed that the stretching lineations associated with the amphibolite facies metamorphism are NW-SE trending and associated with penetrative top to the NW shear bands. It has been interpreted as reflecting the gravitational collapse of the EPO at Silurian times. Another direction of stretching highlighted in the whole massif by these authors is a horizontal NE-SW trend in average. It is associated with strain localization into mylonitic shear zones, also under amphibolite facies conditions, at the boundary between the high-grade rocks and greenschist facies rocks. The structural and spatial relationships or distribution of the two distinct directions of stretching have never been studied or discussed. Kinematics associated with the second family of lineations are not well-constrained as they can be either extensional following J. Wang et al. (1994), sinistral after Y. J. Wang, Fan, Cawood, et al. (2007), or mainly dextral for Lin et al. (2008). Furthermore, these high-grade and high-strain fabrics were interpreted as Early Paleozoic by J. Wang et al. (1994) while Lin et al. (2008) argue for a Triassic age. More recently, petrological and geochronological studies by C. H. Chen et al. (2011, 2017), X. Wang et al. (2020), and Y. J. Wang et al. (2021) highlighted that the Triassic metamorphism was strong enough to crystallize new monazites, apatites, and zircons grains within the basement (Figure 2a), suggesting that (a) some occurrences of migmatites may be Triassic in age, (b) the main amphibolite facies ductile fabrics within the basement are probably Triassic and (c) the Early Paleozoic fabrics were probably totally erased. In addition, the vicinity of the Yunkai massif and its associated peripheral Late Paleozoic basins were also reworked by NE-SW striking greenschists facies dextral or reverse shear zones (J. Li, Zhao, et al., 2017; Lin et al., 2008; Ni et al., 2019; K.-J. Zhang & Cai, 2009). After J. Li, Zhao et al. (2017), north-westward thrusting along the Qin-Fang Shear Zone (QFSZ, Figure 2a) occurred at least since ca. 253 Ma (i.e., synchronous with granulite facies metamorphism; L. Zhao et al., 2010). There, the Shiwandashan turbiditic basin was filled by the dismantled 260–240 Ma magmatic rocks from the core of the Yunkai massif and evolved from deep marine to terrestrial environments (Hu et al., 2015). Within the massif, most of the strike-slip shear zones, like the Luchuang-Qinxi Fault (LQF) and the Luoding-Yuecheng Fault (LYF), were mainly dated by $^{40}Ar/^{39}Ar$ at ca. 230–205 Ma (Y. J. Wang, Fan, Cawood, et al., 2007; Y. J. Wang et al., 2021; K.-J. Zhang & Cai, 2009; Figures 2a and 2c) or locally at ca. 180 Ma (Ni et al., 2019).

3. Methodology

3.1. Field Observation and Sampling

For this study, petrographic, structural, and kinematic analyses were performed throughout the Yunkai massif. Planar, linear fabrics, and kinematic criteria related to the emplacement of anatectic rocks and the deformation in the massif were systematically measured. This study mainly focused on several key areas located along the coast, where outcropping conditions are outstanding, giving an almost continuous cross-section of the migmatitic mid-lower crust. Representative geological and structural features are described at Fuhu Hill, Shapa Bay, Jiahai Bay, and Hailing Island (locations in Figure 3). We propose new geological maps of the studied areas, coupled with regional to local structural maps and cross-sections. Additional structural data and inland cross-sections (Longgaoshan Mountains, location in Figure 3) are available in Figure S1. Besides, 63 samples were collected for petrographic and microstructural analyses. Thin-sections were prepared normally to the schistosity and parallel to the mineral-stretching lineation (*XZ* planes).

Among these samples, we selected representative samples of magmatic and metamorphic rocks for U-Pb dating on zircons to constrain the magmatic event and its associated tectonics in the southern Yunkai massif (see the precise locations of samples in Figures 3, 7, 9, and 11). We chose one diatexite (21BCOCS24) from Jiahai

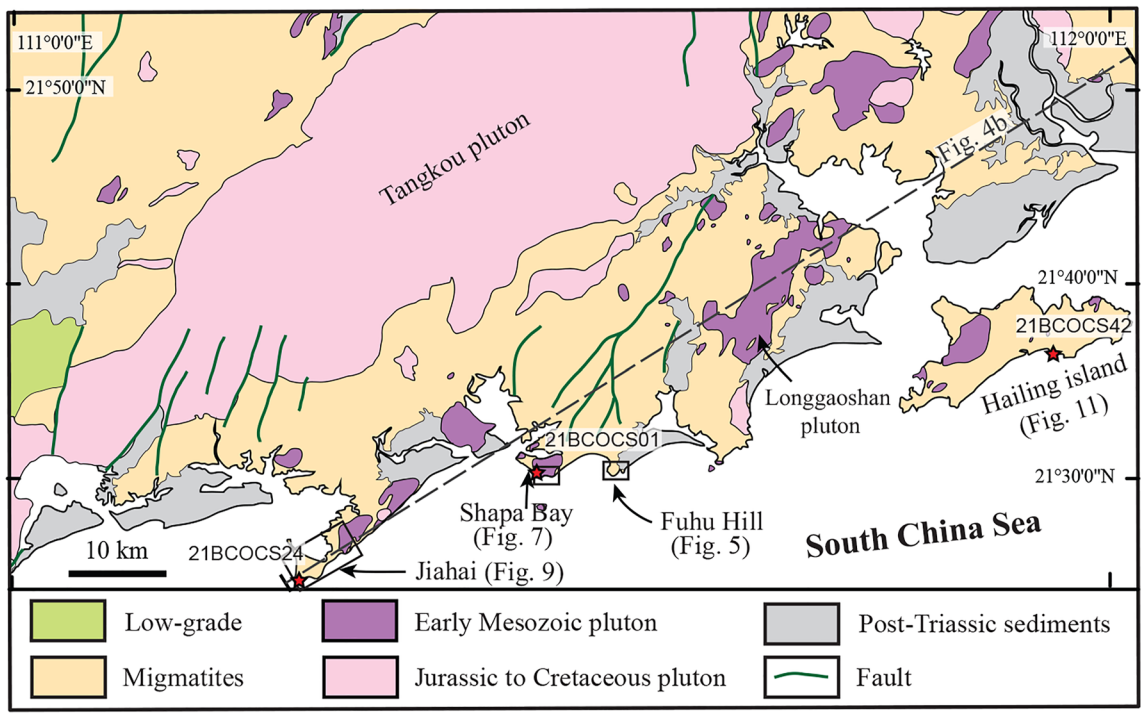

Figure 3. Geological map of the south of the Yunkai massif. The different studied areas are highlighted.

Bay, one late-kinematic (i.e., weakly deformed compared to the country-rocks) porphyritic granite from Shapa Bay (21BCOCS01), and the late-kinematic porphyritic Dinahai granite from Hailing Island (21BCOCS42), as geochronological study was never carried out there, contrary to Fuhu Hill.

3.2. Geochronology

Zircon grains were obtained from crushed rocks using standard mineral separation procedure. Zircons grains were extracted from powders using heavy liquids, electric and magnetic separation techniques. Colorless, unbroken, and transparent single zircon grains were handpicked under a binocular microscope, embedded in epoxy mount and polished to half of their original thickness. About 60–80 zircon crystals were imaged by cathodoluminescence (CL) using a Quanta 400 FEG scanning electron microscope equipped with a Gatan mini-CL detector (Mono CL3+) at Nanjing Hongchuang Geological Service. Transmitted and reflected images were also taken by an optical microscope to better image the morphology and inclusions of zircons.

U-Pb analyses were performed by LA-ICP-MS at the State Key Laboratory for Mineral Deposits Research of Nanjing University. A Coherent GeoLas Pro ICPM was used, coupled with a New Wave 193 nm laser ablation system. The full instrumental conditions and dating processing are available in Table S2. The analytical results are presented in Table S3.

4. Results

4.1. Structural Patterns and Kinematics

4.1.1. Large Scale Analysis

The migmatitic complexes from the south of Yunkai form elliptical domal structures, which are defined by the main penetrative planar fabric that form a regional foliation. Foliation trajectories show that these domes are elongated along a NE-SW trend (Figure 4a). This NE-SW trend, which is consistent with the main structures of the Yunkai massif (Figures 1 and 2) will be called hereafter as the main "orogenic" trend. The cores of the domes are made of discontinuous lenses of diatexites (i.e., more than 50% of melt fraction) and are mantled by metatexites

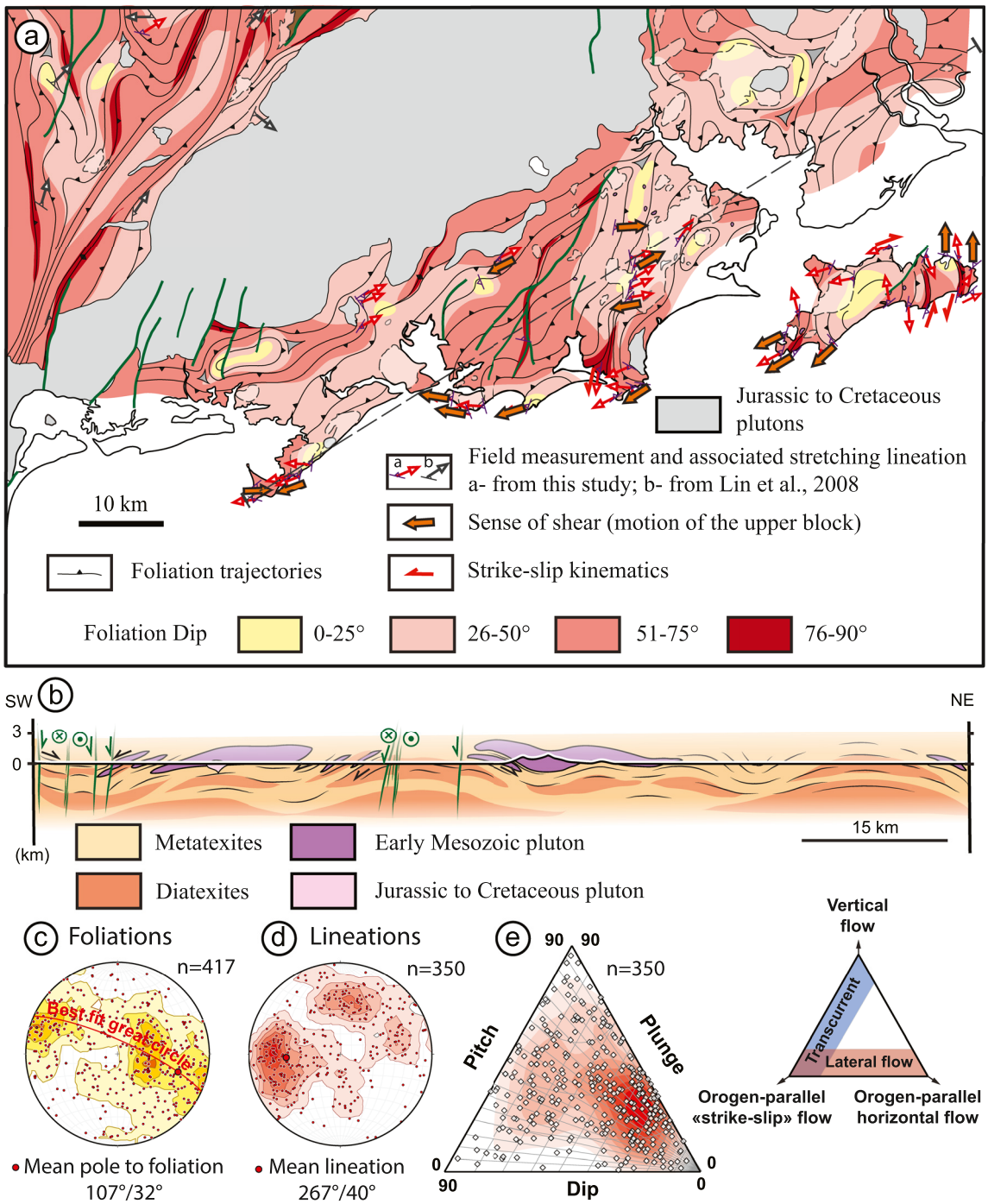

Figure 4. Main structures of the studied area: (a) structural map of the south Yunkai massif. The foliation trajectories were drawn after structural measurements from BGMRGD (1988) and Lin et al. (2008) and our own measurements. (b) NE-SW cross-section of the migmatitic complex. Structural measurements from this study: (c) stereogram of the foliation planes, (d) stereogram of the mineral-stretching lineations, (e) dip-pitch-plunge ternary diagram highlighting the crustal flow mode in the studied area (Chardon et al., 2009, after Balé & Brun, 1989).

(Figure 4b). The foliation planes generally have moderate to high dips while low dip values are restricted to the hinge of the domes (Figure 4a). Scattering of the poles of our measurements on an ENE-WSW trend attests to an NNE-SSW trend of domes along the coast (Figure 4c). The upper parts of the gneiss domes are intruded by several batholiths and smaller plutons, both having a laccolithic shape (Figure 4b).

The regional foliation bears a mineral-stretching lineation defined by quartz ribbons, oriented or elongated feldspars, fibrolitic sillimanite, or aligned biotite flakes or aggregates. The lineations have a dominant E-W to NE-SW trend in map view (Figure 4a). Our measurements highlight a dominant E-W (i.e., 267°) trend and a secondary N-S to NE-SW trend of lineations plunging to the N to NE (Figure 4d). In detail, the mineral-stretching lineations are mostly down-dip on foliation planes, falling in the "low dip-low plunge-high pitch" of the ternary diagram, that is, close to the "orogen-parallel horizontal flow" pole (Figure 4e). In the whole studied area, regional stretching is associated with the activation of shear bands showing systematic down-dip sense of shear (i.e., extensional; see the next sections for details). Opposite kinematics are observed on each edge of gneiss domes, with top-to-the-W to SW kinematics and top-to-the-E to NE kinematics at the SW and NE vicinity of gneiss domes, respectively (Figures 4a and 4b). The scattering of lineations toward higher dip and moderate pitch domain (i.e., toward the "orogen-parallel strike-slip flow" pole), suggesting local transcurrent deformation (Figure 4e). Such low-pitch lineations are mostly localized at the limbs of gneiss domes while high pitch lineations are mostly observed in the core and at the NE or SW borders of gneiss domes (Figure 4a). The vertical component of shear remains extensional while the strike-slip component depends on the location on each limb of the gneiss domes. The south-eastern and north-western limbs exhibit sinistral component of shear while the two others are characterized by dextral one (e.g., Longgaoshan, Hailing Island; Figure 4a).

The massif is cross-cut by late NNE-SSW to NE-SW striking faults, which are almost parallel to the long axis of gneiss domes (Figure 4a). The main faults are steeply dipping contrary to the regional foliation and exhibit dextral kinematics or vertical displacement (Figure 4b). These late brittle-ductile faults are described in detail in the following sections.

4.1.2. Fuhu Hill: An Anatectic Core

This massif is essentially composed of diatexites, developed at the expense of metasedimentary rocks (Figure 5a). Migmatitic orthogneiss was observed only at the easternmost part of Fuhu Hill (Figure 5a). Within diatexites were locally preserved some metatexites lenses at the central part of the massif. The proportion of intrusive magmatic rocks increases westward, with a large amount of pegmatites and at the westernmost part of the massif, as well as small sheets of biotite granites (Figure 5a). Boudins or septas within migmatites are common and include amphibolitic mafic rocks, as exemplified by Z. Chen et al. (2021).

Most of the massif is characterized by low strain fabrics (i.e., magmatic fabrics). Despite that migmatites are highly folded, the foliation has a consistent N-S to NNE-SSW strike and is shallowly to moderately dipping to the west (Figures 5b and 5d). Strain localization within meter to decameter shear zones can be recognized at the top of migmatitic orthogneiss, within the metatexite lenses and their surrounding diatexites (Figures 5a and 5g). The foliation within the shear zones is concordant with the surrounding magmatic foliation. Strain localization is well expressed by the transition from highly folded metatexites to extremely banded metatexites-diatexites alternations showing mylonitic fabric (Figures 5g and 5h). Within the shear zones, pegmatites and leucosomes are sheared and boudinated (Figure 6a). Isoclinal and sheath folds are commonly observed in the shear zones. Mylonitization seems to heterogeneously affect the diatexites. Indeed, while most of the metatexites show high strain fabrics, their surrounding diatexites locally crosscut the mylonitic foliation (Figure 6b). Sheared leucosomes also evolve laterally as vertical pegmatitic or granitic dykes crosscutting the foliation (Figure 6c). These observations suggest that the deformation and emplacement of the migmatites were coeval. The main granitic sills located to the west show migmatitic textures at their boundaries and the foliation is mostly concordant with the one observed in the surrounding migmatites (Figure 6d).

Mineral stretching lineations have a regular WSW-ENE trend and low plunge (Figures 5c and 5e). Magmatic lineation within granitic sheets is similar to the one in their country rocks (Figure 5c). More precisely, lineations are mostly down dip (i.e., high pitch on foliation planes) and can have a moderate pitch, falling into the "orogen-parallel horizontal flow" pole. There are no differences in lineation trends between low strain and high strain zones. Between the shear zones, the foliation within the alternation of metatexites and diatexites is highly folded, with a fold axis parallel to the direction of stretching (Figures 5b and 5g). Shear bands are common in the migmatites, even in low strain domains and most of them show top-to-the-west kinematics (Figure 6e). Meter-scale antithetic slip boudinage (i.e., domino-like) is well expressed within the mylonitic metatexites and is compatible with top-to-the-west shearing (Figure 5h). Decimeter to meter-scale asymmetrical folds are also compatible with top-to-the-west shearing. Inter-boudins and shear bands are filled by fabric-free leucosomes or pegmatites, attesting that deformation occurred during partial melting. Where lineations have a moderate

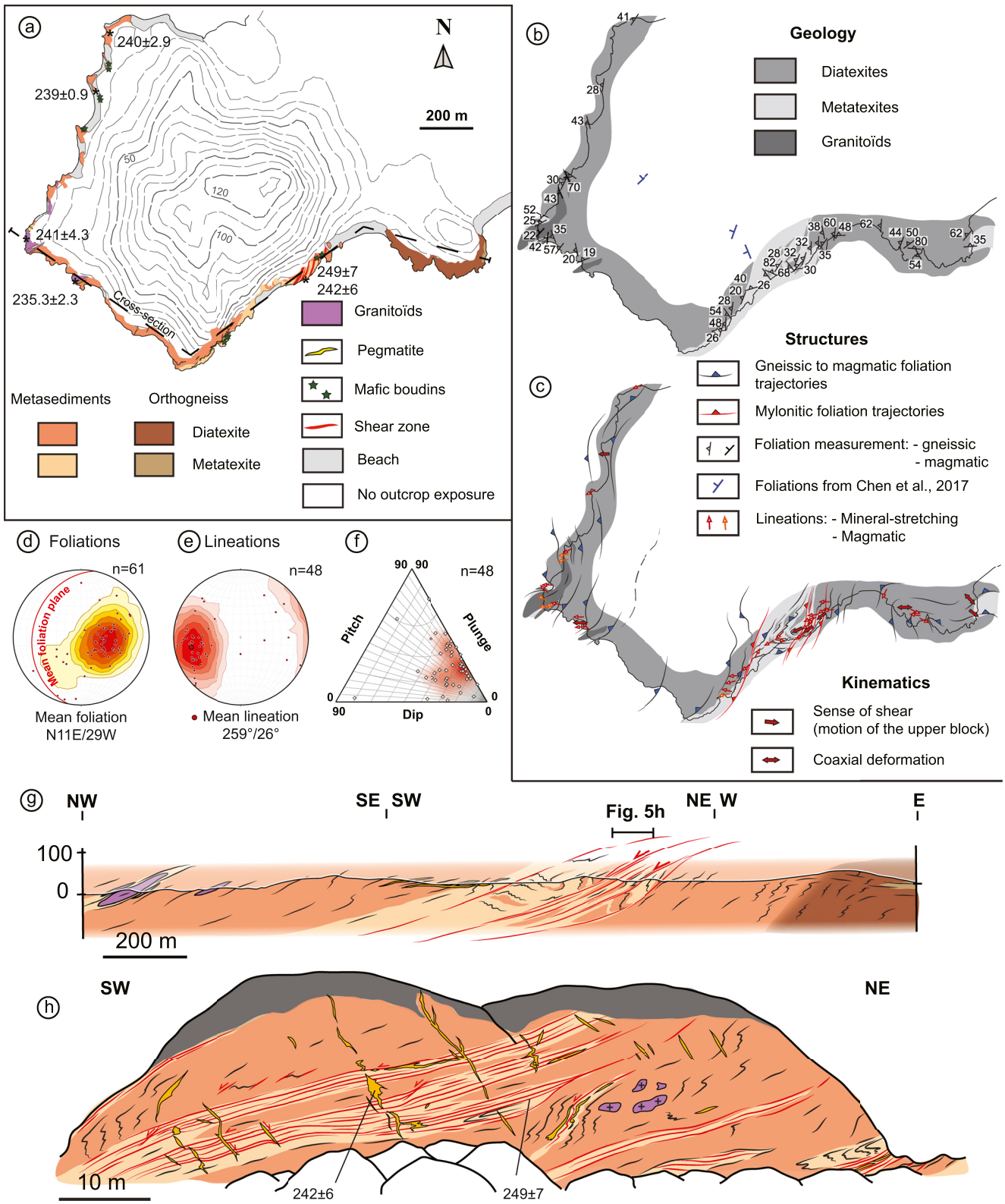

Figure 5. Geological and structural features of Fuhu Hill area. (a) New geological map of Fuhu Hill; (b and c) structural maps of Fuhu Hill, highlighting the trend of the regional foliation and mineral-stretching lineations, respectively; stereograms of (d) foliation planes and (e) lineations; (f) dip-pitch-plunge ternary diagram; (g) cross-section through Fuhu Hill (location in (a)); panorama of the metatexites-diatexites alternation and associated strain localization (location in (g)). Available U-Pb ages are located and are from Z. Chen et al. (2021), Y. J. Wang et al. (2021), and J. Zhang et al. (2019).

10.1029/2022TC007457

Figure 6. Photographs of migmatites and granites from Fuhu Hill. (a) Banded (mylonitic) metatexites showing asymmetrical boudinage in response to top-to-the-west shearing. (b) Example of diatexites crosscutting the banded metatexites. (c) Channeling of granitic melts from horizontal leucosomes to vertical dykes. (d) Contact between metatexites and dirty biotite granite sills from the western part of Fuhu Hill. Biotite granite exhibits migmatitic xenoliths and a magmatic foliation that is concordant with the one in the migmatites. (e) Sheared leucosomes (top-to-the-west C' shear planes) in diatexites. (f) Conjugated C' shear planes in diatexites from the eastern part of Fuhu Hill.

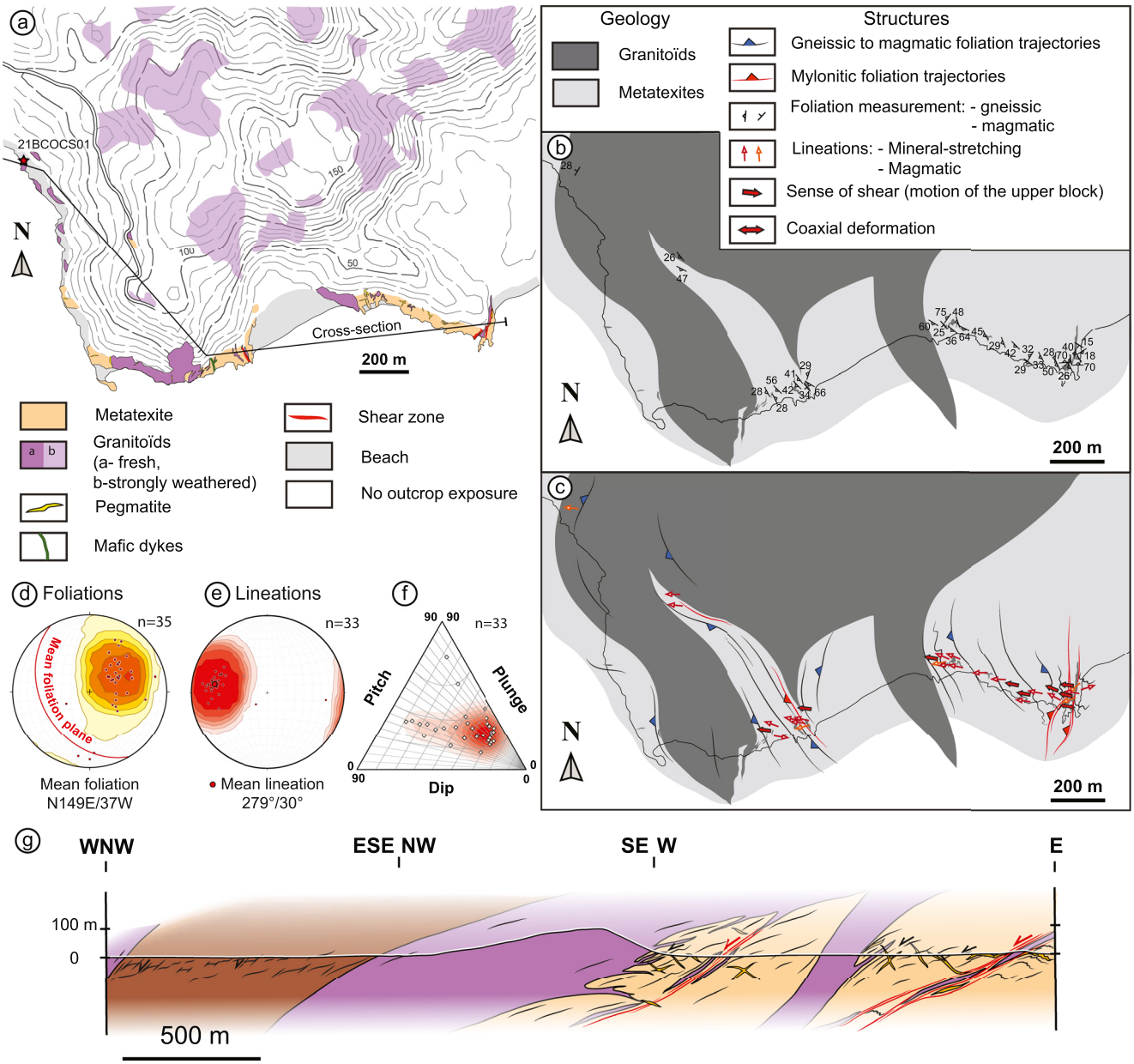

Figure 7. Geological and structural features from Shapa Baya area (location in Figure 3): (a) new geological map; (b and c) structural maps of Shapa Bay showing the foliations planes (b) and mineral-stretching lineations (c); stereograms of (d) foliation planes and (e) mineral-stretching lineations; (f) dip-pitch-plunge ternary diagram; (g) cross-section of Shapa Bay (location in (a), the cross-section continues 1 km westward).

pitch, the horizontal component of shear is sinistral. However, symmetrical boudinage and conjugate shear bands showing both top-to-the-west and top-to-the-east kinematics can be observed (Figure 6f). These structures are interpreted as reflecting local coaxial deformation (Figure 5c).

4.1.3. Shapa Bay: A Feeding Zone of Plutons

The Shapa Bay forms the western continuity of the Fuhu Hill (Figure 3). The eastern part of the Bay is made of metasedimentary metatexites intruded by a biotite granite (Figure 7a). The shoreline corresponds to the southern end of the pluton that crops on the whole hill (Figures 7a and 7b). There, the metatexites are characterized by shallowly dipping foliation planes having an NNW-SSE strike (Figures 7b and 7d). Like in the Fuhu Hill, strain was heterogeneously accommodated within the migmatites, where folded migmatites form low strain zones, while extremely banded migmatites characterize the main shear zones. These decimeters to meter-thick shear

zones are mainly localized at the boundary with or within pegmatites (Figure 8a) or at the vicinity of the main pluton. Pre-kinematic (i.e., highly sheared), syn-kinematic (weakly deformed) to late-kinematic (oblique and undeformed) pegmatitic dykes are commonly observed. The amount of dykes increases toward the bottom of the main granitic pluton (Figures 7a and 7g). The south-eastern part of the granitic intrusion forms a hundred-meter-thick dyke, slightly oblique to the main foliation in the country rocks, while the western sheet of granite forms a 500 m thick laccolith. The core of the pluton is characterized by a weak magmatic foliation that is concordant with the foliation of its country-rocks. The pluton can have a mylonitic fabric at the boundary with the migmatites. The western part of the cross-section along the Shapa Bay (i.e., at the top of the pluton) is made of ca. 700–800 m thick migmatitic porphyritic orthogneiss (Figures 7g and 8b).

Mineral-stretching lineations within migmatites have a consistent N280°E mean trend in the whole area (Figures 7c and 7e), which is parallel to the observed fold axis. The pluton exhibits a mineral lineation with the same trend, defined by well-oriented feldspar phenocrysts (Figure 8c). Mineral-stretching lineations have a high to moderate pitch on foliation planes and are clustered in the "orogen-parallel horizontal flow" pole (Figure 7f). Both the low strain zones and the main shear zones show similar top-to-the-west kinematics (Figures 7c, 7g,, and 8d). Within the pre-tectonic orthogneiss located at the top of the pluton, strain appears as homogeneous, with regularly spaced shear bands (C/S-like fabric, following Gapais, 1989) between each feldspar phenocrysts (Figure 8b). Shear bands have an average angle of ca. 20°–25° with the foliation. It suggests a minimum amount of shear γ equal to ca. 2 (i.e., 200%) under simple shear (see Ramsay, 1967).

4.1.4. Jiahai Bay: A Termination of Two Gneiss Domes

The migmatites from the Jiahai Bay show a low amount of melt products and diatexites are restricted to decameter to hundred-meter thick lenses within metatexites (Figures 9a and 9b). Like in the Shapa Bay, several hundred-meter thick laccolithic plutons intrude the migmatites (Figure 9b). The migmatites are dominantly shallowly dipping with an overall NNW-SSE strike (Figures 9a–9c). The main foliation dips to the east or west in the western and eastern parts of the bay, respectively (Figure 9b). The central part of the bay is characterized by sub-horizontal fabrics. Thus, the eastern part of the Jiahai Bay is likely to form the western termination of the gneiss dome centered on the Fuhu Hill (Figure 4). Foliation planes bear well-defined ENE-WSW trending mineral-stretching lineations in the whole area (Figures 9a and 9d). These lineations have dominantly a high pitch on the foliation planes and fall in the "orogen parallel horizontal flow" pole, slightly scattering toward the "strike-slip" pole (Figure 9e). The migmatites show low strain fabrics and deformation looks homogeneously accommodated. Migmatites are folded, with fold axes parallel to the mineral-stretching lineation and show discrete C' shear bands. The kinematics associated with the shear bands are mostly extensional, with top-to-the-east and top-to-the-west sense of shear in the western and eastern part of the bay, respectively. However, conjugate sets of shear bands are common in the western part of the bay (Figures 8e and 9a) while no kinematics has been found in the central part, suggesting coaxial deformation at the transition between the eastern and western domal structures. Fabric-free granitic veins and tourmaline-quartz veins are frequently observed within shear bands, attesting that deformation occurred during partial melting like in the rest of the studied area.

The transition from one dome to another in this area is disturbed by late greenschist facies mylonitic shear zones. These shear zones are meter to hundred-meter thick and in NNE-SSW to NE-SW striking (Figures 9a and 9f). Almost all the shear zones are vertical (Figures 9b and 9f). Two sets have been recognized, depending on their kinematic and structural relationships (Figures 9a and 9b). The first set has low-pitch striae-lineations (Figure 9f) and the associated C' shear bands show a dextral sense of shear (Figures 9a and 10a). The main dextral shear zone is located at the western-central part of the bay with a thickness of ca. 100 m. The shear zone is responsible for the intense folding (i.e., isoclinal) of the primary migmatitic fabric but the impact of the shear zone vanishes after few meters around, where sub-horizontal migmatitic and magmatic fabrics can be appreciated. The second set of shear zones forms decimeter to meter-scale mylonites (Figure 10b) and has down-dip striae-lineations (Figure 9f). The deformation is mostly ductile but can evolve under brittle conditions. The shear zones have vertical movement, showing mostly east-side up kinematics (Figures 9a, 9b, and 10b'). Only one shear zone was moderately dipping to the east and exhibits top-to-the-west (i.e., reverse) kinematics (Figure 9a). The inflection of the primary foliation in the migmatites is observed only over ca. 1 m outside the shear zones. The relative chronology of these two sets can be deciphered in the western-central part of the bay. Indeed, the second one was developed at the expense of the core of the first one under brittle-ductile conditions, reworking the low-pitch

10.1029/2022TC007457

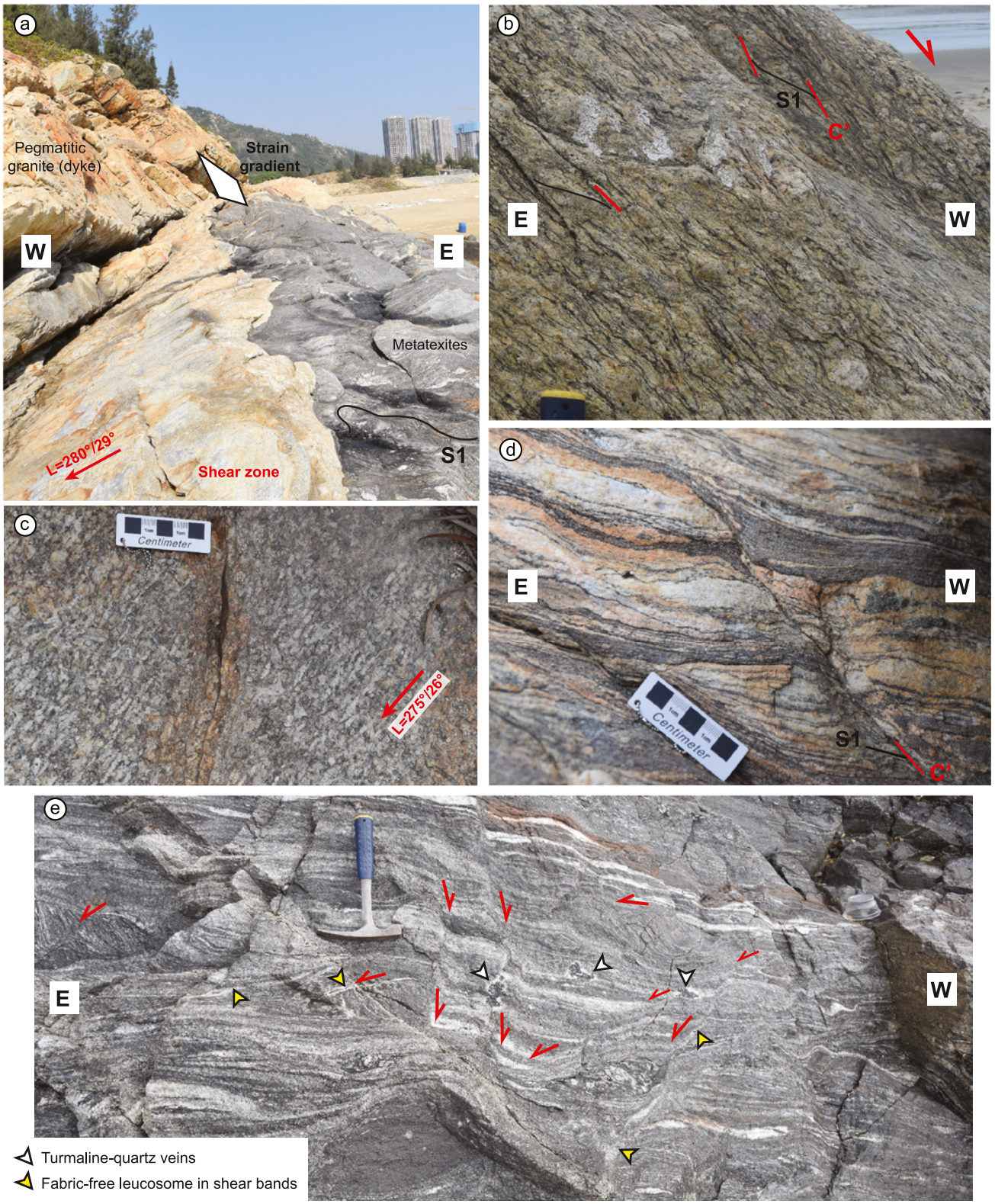

Figure 8. Photographs of migmatites and granites from Shapa and Jiahai bays: (a) example of strain localization at the base of pegmatites (Shapa Bay); (b) migmatitic orthogneiss showing C/S structures compatible with top-to-the-west shearing (Shapa Bay); (c) magmatic foliation of porphyritic granite from Shapa Bay; (d) C' shear plane in metatexites, showing top-to-the-west kinematics (Shapa Bay); (e) conjugated shear planes with injection of leucosomes and Turmaline-quartz veins within (Jiahai Bay).

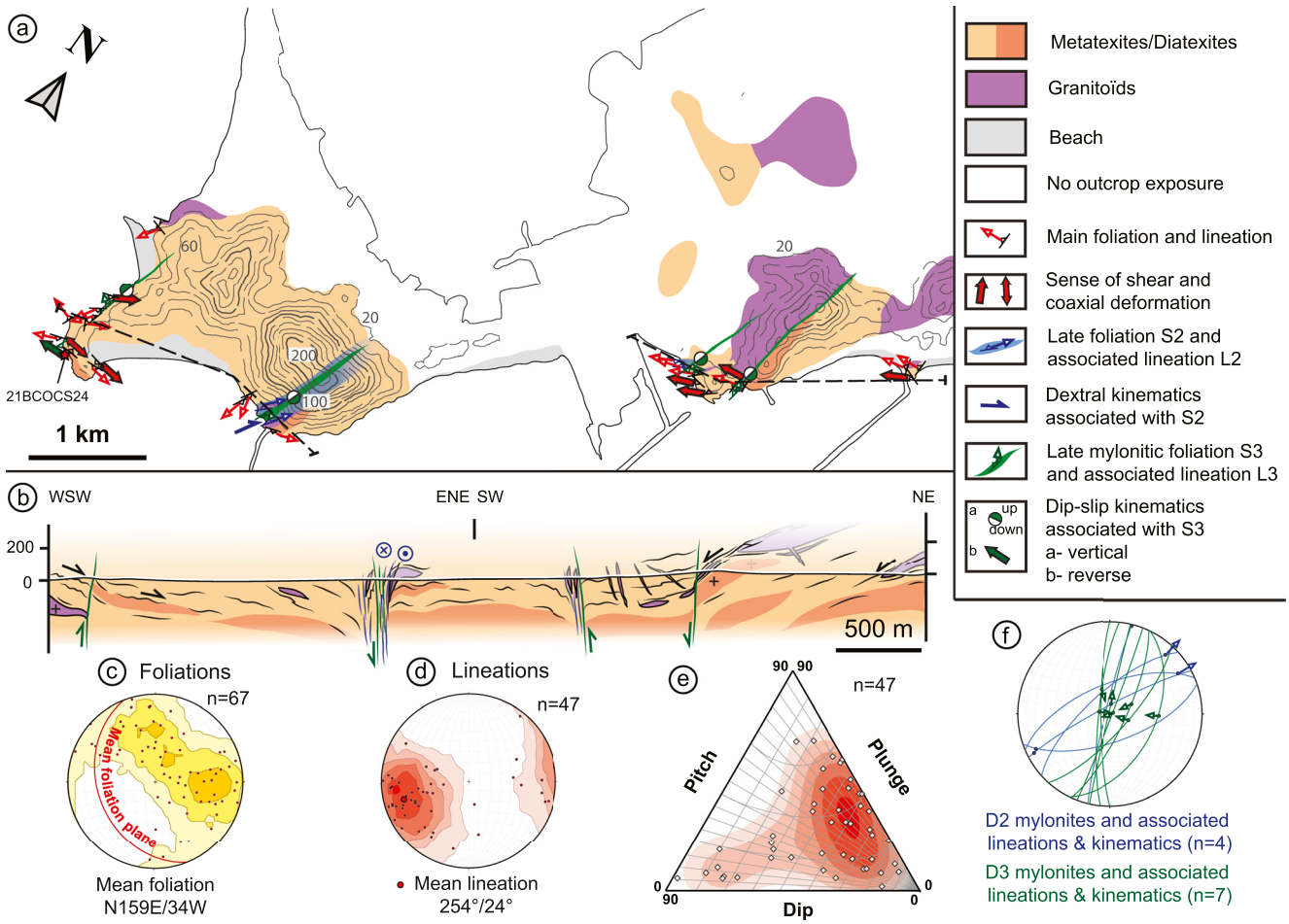

Figure 9. Geological and structural features from Jiahai Bay: (a) new geological map and associated measurements of foliations and lineations; (b) cross-section of the area (location in (a)); stereograms of (c) foliation planes and (d) mineral-stretching lineations (S1/L1); (e) dip-pitch-plunge ternary diagram of L1 measurements; (f) stereogram of the late mylonitic shear zones (D2 and D3).

striae-lineations. The dextral shear zones were thus developed before the second set of narrow shear zones and will be described in the rest of the article as referred to distinct D2 and D3 deformation events, respectively.

4.1.5. Hailing Island: An Almost Complete Gneiss Dome

The Hailing Island, located at the eastern part of our studied area (Figure 3), forms an NE-SW elongated gneiss dome (Figures 11a and 11b). The Hailing dome is incomplete as its southern part has been fully dismantled by the South China Sea (Figure 11b). Metatexites and diatexites characterize almost the whole massif. The diatexites form hundred-meter to kilometer thick lenses and are mostly associated with laccolithic sills of granite showing similar size (Figures 11a–11c). The spatial extent of diatexites in the inner parts of the island remains difficult to estimate due to poor outcrop conditions. Interestingly, the easternmost part of the island is characterized by paragneiss and locally metatexites showing a low amount of melt products (Figure 11a). In this area, white micas can be observed, contrary to the rest of the whole studied area (i.e., biotite migmatites). The main foliations within the gneiss dome have an NNE-SSW strike (Figure 11d), which is quite oblique to the long axis of the dome (Figure 11b). It can be explained by the fact that the best-exposed areas (i.e., preserved) are the opposite eastern and western terminations of the dome (Figure 11b). The foliation planes are dominantly steep to vertical (Figure 11d), and shallowly dipping foliation planes were mostly observed in the core of the gneiss dome (Figures 11a and 11c).

The mineral-stretching lineations within migmatites and granites have an N-S mean trend (Figure 11e). Nevertheless, two different trends can be observed, depending on the location within the dome (Figure 11b). Indeed,

10.1029/2022TC007457

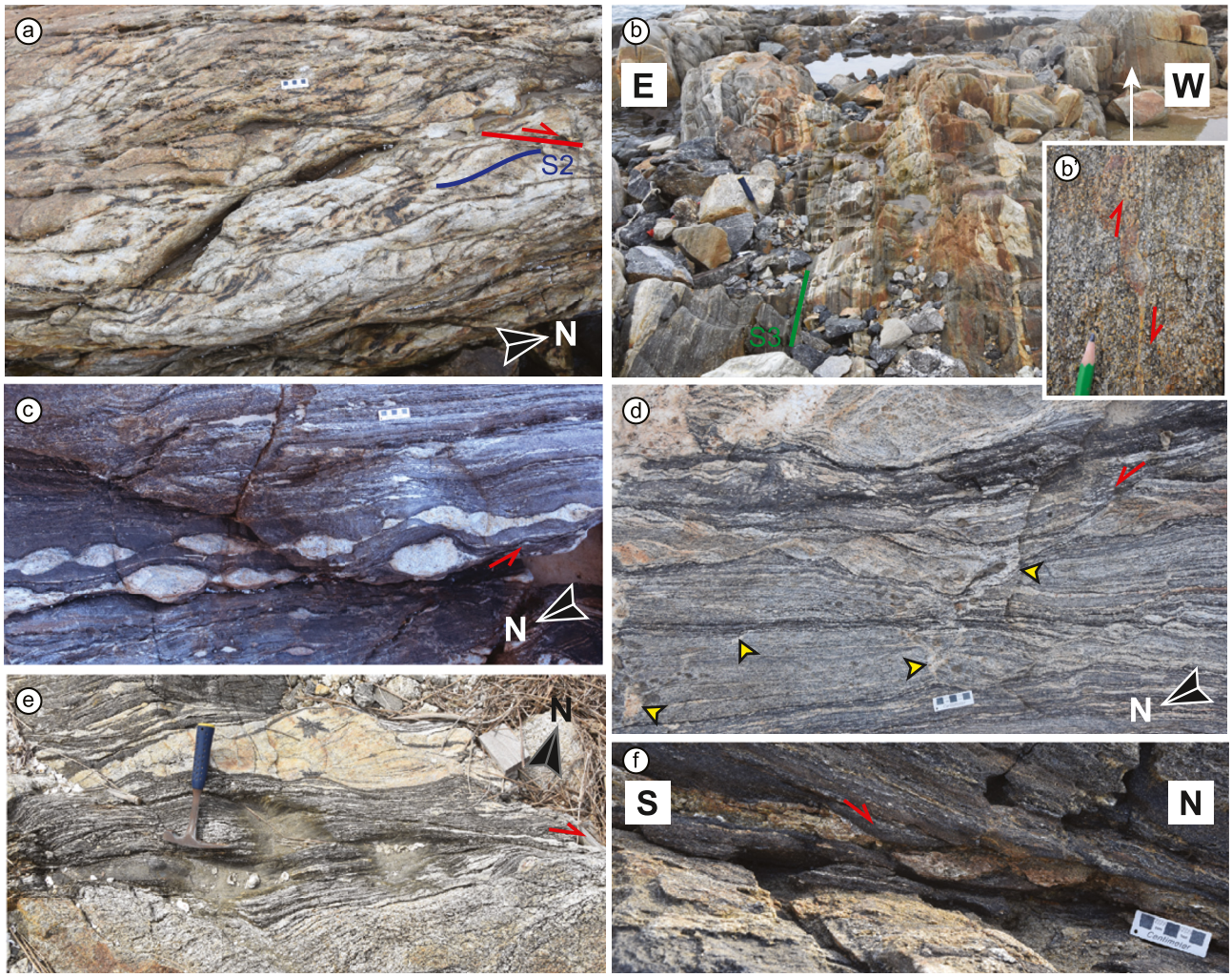

Figure 10. Photographs of sheared migmatites and granites from Jiahai Bay and Hailing Island: (a) leucogranite affected my S2 mylonites with dextral kinematics (Jiahai Bay); (b) steep mylonitic corridor (D3) showing East-side-up kinematics (Jiahai Bay); (c) leucosomes affected by asymmetrical boudinage (C' shear planes with sinistral kinematics) within the East Hailing Island Shear Zones; (d) injection of fabric-free leucosomes within sinistral shear planes and inter-boudins (East Hailing Shear Zones); (e) pegmatite-diatexites-metatexites alternations affected by dextral shearing (north Hailing Island); (f) shallow top-to-the-north shear planes in paragneisses (north of the East Hailing Shear Zones).

the north-western half part of the island shows ENE-WSW trending lineations while the opposite half part shows an NNE-SSW to N-S trend. The subdivision is more or less delineated by the NE-SW striking Linggu fault zone. The mineral-stretching lineations are clustered in the higher-central part of the Pitch-Plunge-Dip ternary diagram as the majority of foliation planes are moderately to steeply dipping (Figure 11f). Lineations have high to moderate pitch (i.e., between 30° and 70°), highlighting that the island is characterized by dominant "vertical flow" to "transcurrent" modes (Figure 11f). In the western part of the island, the diatexites mostly exhibit magmatic flow fabrics (i.e., low strain). The diatexites form steep hundred-meter to kilometer-thick lenses. Within, magmatic lineations are steeply plunging to the SW, suggesting vertical flow of magmas. Within the surrounding metatexites, C' shear bands reveal top-to-the-WSW kinematics (i.e., sinistral-normal).

On the contrary, the eastern part of the island shows strongly heterogeneous deformation. Low strain domain has been only observed near the core of the dome, with dominant NW-SE trending mineral-stretching lineations (Figure 11b). Shear bands are rare but few top-to-the-SE kinematics have been observed. In the rest of the eastern part of the island, strain localization within kilometer-thick shear zones has been highlighted (Figures 11a–11c). As no outcrop was found between these two shear zones, it is not possible to decipher if it constitutes a single ca. 10 km thick shear zone or two distinct shear zones. Here, we will take the second solution in consideration

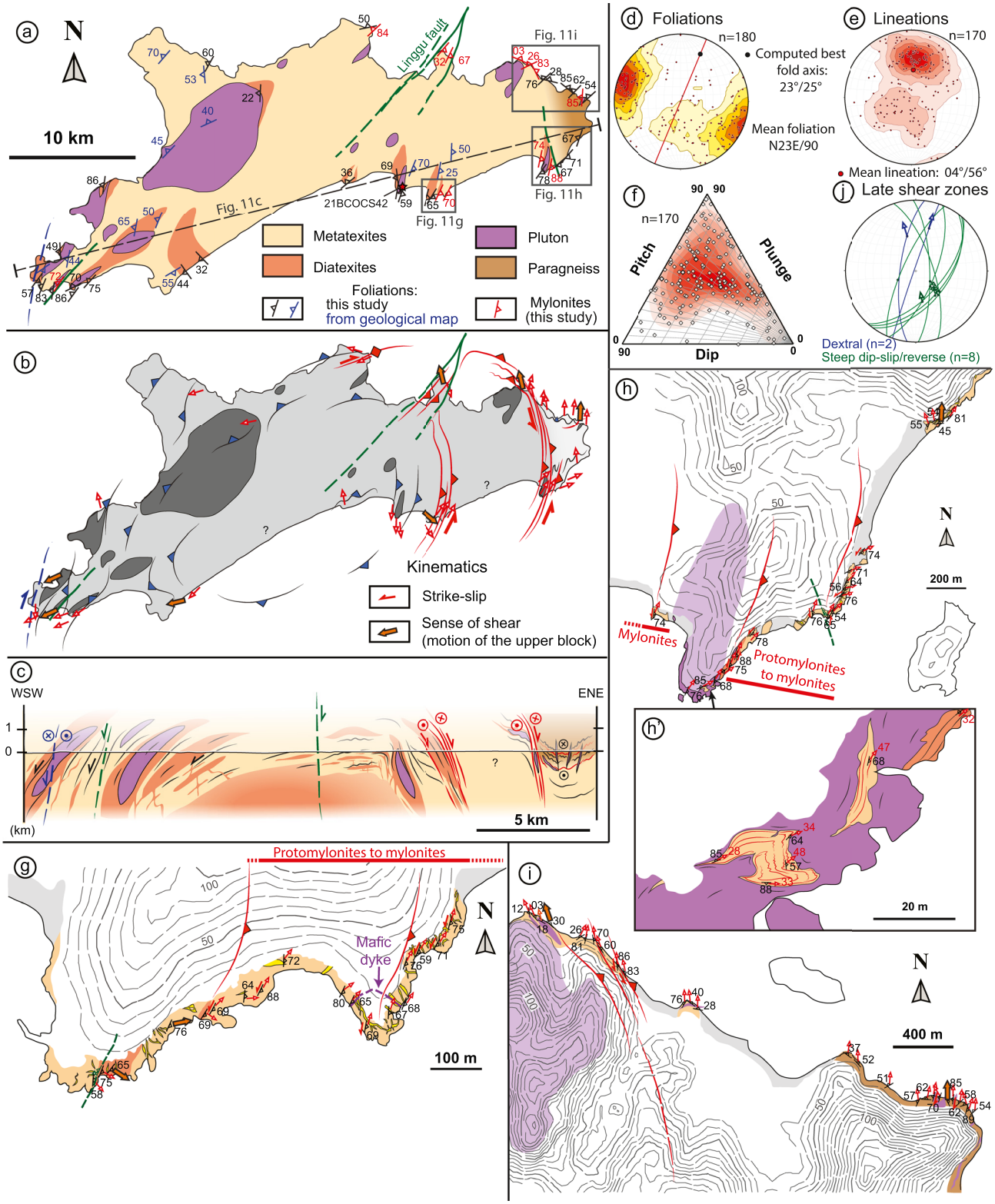

Figure 11. Geological and structural features of Hailing Island: (a) new geological map; (b) structural map of the island; (c) regional cross-section; stereograms of (d) foliation planes (S1) and (e) mineral-stretching lineations (L1); (f) dip-pitch-plunge ternary diagram of L1 lineations; (j) stereograms of late mylonitic shear zones; (g, h, h') and (i) detailed geological maps and structural measurements from the East Hailing Shear Zones (location in (a)).

though the first one remains possible. The shear zones are parallel to the shape of the dome, striking to the NE and turning to the SE in the southern and northern coasts, respectively (Figures 11b, 11g, 11h and 11i). The stretching lineations within the NE and SE striking shear zones are NE-SW and N-S trending, respectively. Hundred-meter thick sills of granites intrude the shear zones (Figures 11b, 11h and 11i). Within the shear zones, migmatites show protomylonitic to mylonitic fabrics while the plutons keep magmatic textures or few occurrences of solid-state deformation. Migmatitic texture is often preserved within the plutons. However, the plutons exhibit mineral-stretching lineations parallel to the one in their mylonitic country-rocks (Figures 11h and 11i). Decameter-scale migmatitic sheath fold-like or sheet septas were observed within the pluton, showing concordant stretching lineations to those observed in the surrounding pluton and the shear zones (Figure 11h, h'). Granitic and pegmatitic dykes are common in the shear zones. These dykes are (a) sheared and parallel to the mylonitic foliation or (b) cross-cutting the mylonitic foliation and perpendicular to the stretching lineation (Figures 11g and 11h). The C' shear bands observed in the shear zones have sinistral kinematics (Figures 10c, 11b, and 11g–11i). A normal (i.e., extensional) component of shearing is associated with strike-slip movement.

Like in the rest of the studied area, deformation occurred during partial melting, as attested by the injection of fabric-free granite veins within the shear zones (Figure 10d). To the north, that is, in the SE striking shear zone, the normal component becomes dominant and is associated with moderate to shallowly north-dipping top-to-the N/NNE shear bands (Figures 10f and 11i). More to the west (i.e., the northern part of the island), the steep ENE-WSW striking mylonitic foliation is associated with dextral kinematics (Figures 10e and 11b). The hanging-wall of the shear zone, which is well visible at the easternmost part of the island, is characterized by weakly molten metasedimentary rocks or two micas paragneiss showing protomylonitic to mylonitic fabrics and interference patterns. Indeed, in this domain, the main foliation is homogeneously folded, with fold axes parallel to the regional N-S trending stretching lineation (Figure 11i). The stretching lineation is extremely well defined, contrary to the foliation, forming L-type structures (i.e., constrictive). Where observed, north-dipping C' shear bands have top-to-the-north kinematics. On the flanks of N-S oriented folds, the kinematics can be dextral or sinistral, depending on if the foliation is west or east-dipping, respectively.

The main primary structures in the migmatites and plutons were locally disturbed by late deformation events like in the Jiahai Bay (Section 4.1.4). It led to the development of decimeter to meter-scale greenschist facies mylonitic shear zones having N-S to NE-SW strikes (Figure 11j). Like the late shear zones previously described, some of them are steep and bear striae-lineations that can be shallowly or steeply plunging (Figure 11j). The first set was rare and these shear zones have dextral kinematics. The other shear zones were mostly steeply dipping to the SE and exhibit top-to-the-NW (i.e., reverse) kinematics. Only the mylonites associated with the Linggu fault zone had east-side-down sense of shear (apparently extensional, Figures 11c and 11j). The regional foliation in migmatites and granites was poorly disturbed or undisturbed around these thin shear zones, except within the Linggu fault zone. There, the shallow high-grade foliation becomes progressively vertical close to the main faults.

4.2. Microstructural Analysis and Deformation Conditions

4.2.1. Plutons and Migmatites

Most of our samples of granites (16/19) exhibit a weakly to well-defined magmatic fabric. The magmatic foliation is mainly defined quartz-biotite matrix showing an average 300 μm–1 mm grain size, and oriented K-feldspars or plagioclase porphyroblasts (Figure 12a). Garnet, tourmaline and zircon are current accessory minerals. Evidence of deformation is highlighted by recrystallization of quartz grains by Grain Boundary Migration (GBM) and the development of myrmekites in K-feldspars porphyroblasts. These processes attest that deformation took place at temperature above ca. 550°C (Fossen & Cavalcante, 2017; Gapais, 1987; Menegon et al., 2006; Stipp et al., 2002). Only three samples, from the eastern Hailing shear zone and its hanging wall, show a well-defined gneissic fabric. In these samples, recrystallization of quartz grains occurred by GBM and Sub-Grain Rotation (SGR). Myrmekites are still observed in K-feldspars. Muscovite is also present, mostly localized within shear bands. These observations suggest retrogressive deformation from sub-solidus conditions to temperatures slightly under 500°C (i.e., the GBM/SGR transition, Stipp et al., 2002).

Within migmatites, the foliation is variably expressed. It is poorly defined within diatexites, which mostly exhibits a coarse-grained magmatic fabric like in the granites. Nevertheless, the foliation is well defined in metatexites. It is marked by a quartz-biotite-plagioclase matrix and a variable amount of fibrolitic to prismatic sillimanite,

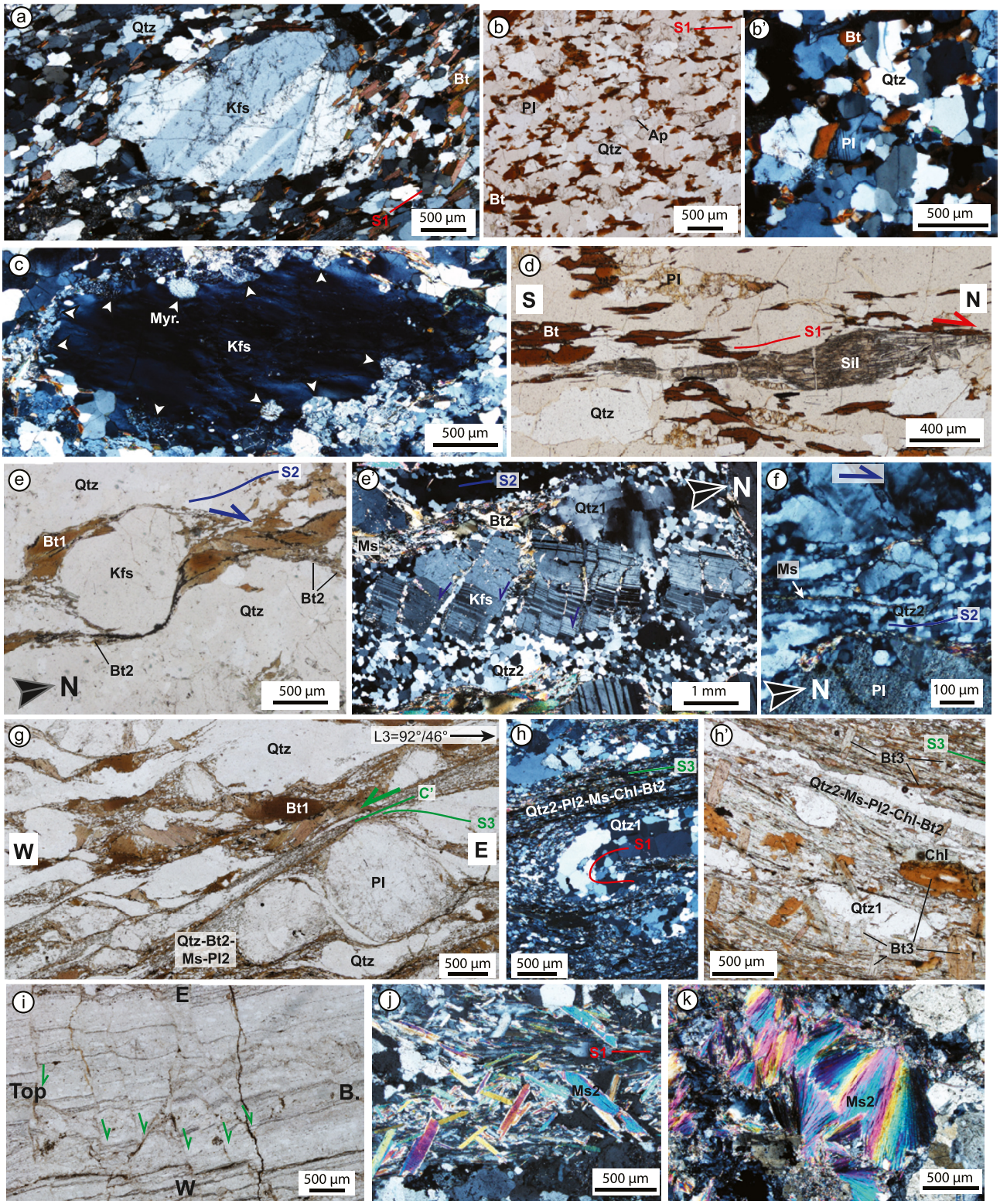

Figure 12.

garnet, k-feldspar, cordierite, apatite, and zircon. Within highly banded migmatites (i.e., mylonites), the fabric is fine-grained, showing a homogeneous matrix of quartz-biotite-plagioclase with an average grain size of 200–300 μm (Figure 12b, b'). The porphyroclasts of K-feldspars show myrmekites recrystallization at crystal boundaries (Figure 12c) and prismatic sillimanites are boudinated along the direction of stretching (Figure 12d). Quartz grains frequently exhibit chessboard microstructures and are recrystallized by GBM (Figure 12b'). Pinning effect of biotite on quartz grains is currently observed (Figure 12b'). These observations are compatible with temperature of deformation above 550°C in migmatites (Hirth & Tullis, 1992; Stipp et al., 2002). Like for plutons, the samples of migmatites from the eastern Hailing shear zones show evidences of retrogressive deformation as highlighted by recrystallization of quartz grains by GBM and SGR, and crystallization of muscovite in shear bands.

4.2.2. Late Shear Zones

Strain localization within D2 dextral mylonitic corridors is highlighted by progressive annealing of primary magmatic or migmatitic textures. At the vicinity of the shear zones, this overprint is characterized by strain localization within shear bands at the boundary of K-feldspar or plagioclase porphyroclasts, mostly within biotite-rich layers (Figure 12e). Large primary biotites (Bt1) are recrystallized into new fine grains (Bt2) (Figure 12e). The feldspar porphyroclasts do not show any recrystallization and are only affected by kink or fractures (Figure 12e'). The fractures, perpendicular to the stretching direction, are filled by new quartz grains (Figure 12e') while tension gashes are mostly filled by muscovite, chlorite or carbonates. The large primary quartz ribbons (Qtz1) are recrystallized into 50–100 μm grains by SGR (Figure 12e'). Quartz ribbons show undulose extinction and deformation lamellae (Figure 12f). In the core of the mylonitic corridors, quartz are recrystallized into fine 10–30 μm grains by Bugling (BLG) and are associated with crystallization of muscovite within shear bands (Figure 12f). These observations suggest that ductile deformation occurred close to the transition between SGR and BLG and with brittle feldspars, that is, close to 400°C and under 450°C (Fossen & Cavalcante, 2017; Gapais, 1989; Stipp et al., 2002). The chlorite or carbonate-rich tension gashes and recrystallization by BLG in the core of the shear zones suggest retrogressive deformation, which may continue at temperature lower than 400°C.

Strain localization within D3 mylonitic corridors shares similar characteristics as for D2 ones. Indeed, the strain is also first localized into biotite-rich layers and at the boundaries of feldspar porphyroclasts (Figure 12g). The D3 deformation is similarly associated with the recrystallization of primary parageneses into a fine-grained matrix made of quartz, new biotites (Bt2), muscovite, and plagioclase, but appearing smaller in grain size, around ca. 10–20 μm (Figure 12g). Feldspar porphyroclasts only exhibits brittle deformation. The primary fabric is progressively erased and only few transposed quartz ribbons remain within the core of the shear zones (Figure 12h, h'). In our samples, the quartz grains are recrystallized by BLG (Figure 12h). Within mylonites and ultramylonites, the grain size reduction is also associated with the crystallization of chlorite (Figure 12h, h'). Within ultramylonitic quartz-rich layers, quartz blasts are 5–10 μm large, and deformation turned to brittle, with the development of antithetic (i.e., dominos) fractures (Figure 12i). These petrological observations and associated microstructures suggest that deformation started under ductile conditions, under 400°C, and ended with brittle quartz, that is, under 300°C (e.g., Fossen & Cavalcante, 2017).

Figure 12. Microphotographs from the various rocks of the South Yunkai massif. (a) Si magmatic foliation within biotite porphyritic granite (Sample 21-BCOCS42, Hailing Island); (b) homogeneous grain size (ca. 200 μm); within mylonitic metatexites (Shapa Bay); (b') same sample under polarized and analyzed light, highlighting Grain Boundary Migration recrystallization of quartz grains; (c) formation of myrmekites at the boundaries of a K-feldspar porphyroclast, within metatexites (same sample than (b and b')) (d) boudinated sillimanite with top-to-the-North kinematics (location: north Hailing Island); (e) partially recrystallized diatexites by late D2 dextral shearing. Primary biotites (Bt1) are recrystallized into fine secondary biotites (Bt2) within shear planes (location: Jiahai); (e') a totally recrystallized biotite granite by late dextral shearing. Quartz ribbons show sub-grain recrystallization into fine neograins (Qtz2), fractured feldspar and new formed white micas and biotites (Jiahai); (f) zoom on the core of the shear planes within late dextral corridors, with grain size reduction of quartz and transition from sub grain rotation recrystallization to Bugling. Primary quartz ribbon (top of the photograph) show undulose extinction and deformation lamellae, which is typically associated with bugling recrystallization (location: Jiahai). (g) Recrystallized diatexites within a late reverse shear zone (D3) from Jiahai Bay (Sample 21-BCOCS24). Primary quartz, biotites and plagioclases are recrystallized into in fine quartz, biotite, muscovite, and plagioclase matrix. (h) Recrystallized metatexites into a D3 steep mylonitic corridor. The primary foliation is partially preserved as folded quartz ribbons while the very fine-grained neoformed matrix is made of quartz, plagioclase, muscovite, chlorite, and biotite (location: east Hailing Island). (h') Evidences of static crystallization of large post-kinematic biotites within an ultramylonitic layer from the sample of (h). (i) Ultramylonitic layers within a steep D3 shear zone from Jiahai Bay. Dominos pattern of cataclasites shows east-side-up kinematics, in agreement with the observed ductile deformation. (j) Evidence of static crystallization of large muscovite within a sheared leucogranite (location: easternmost Hailing Island). (k) Large muscovites filling a fractured and strongly weathered granite (location: Fuhu Hill).

4.2.3. Evidence for Late Metasomatism

The granites, migmatites, and late mylonites observed in the studied area all exhibit evidence for late (i.e., post-kinematic) fluid circulations. It is revealed by the random crystallization (i.e., static) of large biotite, muscovite, and chlorite (Figures 12h' and 12j). These recrystallizations can affect either the Triassic granites, the well-foliated migmatites, or paragneiss and even the D3 mylonites (Figures 12h' and 12j). This is especially observed in mica-rich layers from mylonitic or gneissic samples. Static recrystallization of quartz layers has been also observed in few samples. Nevertheless, static recrystallization remains difficult to decipher within magmatic rocks having sub-isotropic fabrics and could be more widespread. Large post-kinematic micas, like muscovite, can also be associated with the development of fractures, mostly within granites (Figure 12k). In that case, feldspars are strongly weathered and replaced by sericite. All these observations suggest that one or several regional-scale thermal and/or hydrothermal events occurred in the Yunkai massif and were not necessary associated with deformation.

4.3. U-Pb Dating

The results and CL images are presented in Figure 13. Data have been plotted in Concordia diagrams, which have been calculated using Isoplot 3.1 (Ludwig, 2003).

The main population of zircons from the weakly deformed Shapa Bay porphyritic granite (21BCOCS01) consists in euhedral grains with oscillatory zoning, typical of magmatic zircons (Figure 13a). Few other zircons are rounded or irregular (Figure 13a, grains 09, 10, 11). Most of the grains have inherited cores. These cores can show CL-sharp oscillatory zoning (grain 04), homogeneous structure (grains 01, 02), or more rarely sector-zoning (grain 10). The prismatic shape of inherited cores can be preserved (grains 01, 02) or strongly resorbed as highlighted by CL-bright rims crosscutting the internal structures of grains (grains 07, 09, 10). The bright rims evolved continuously to CL-dark rims, with well-defined oscillatory zoning (grains 02, 05, 13). We noticed few occurrences of homogeneous dark rims annealing the internal structure of zircons (grain 11), suggesting recrystallization of primary zircons. The inherited cores yielded concordant $^{206}Pb/^{238}U$ dates ranging from 239 ± 4 Ma to 834 ± 17 Ma (Figure 13b) and five spots gave a Concordia age of 426.4 ± 6.4 Ma (Figure 13c). The euhedral grains with no inherited cores only yielded $^{206}Pb/^{238}U$ dates clustering between 234 ± 5 and 238 ± 5 Ma. The analyzed dark rims gave one concordant $^{206}Pb/^{238}U$ date of 238 ± 4 Ma, which is similar within error to the dates obtained for core-free crystals and from the core of the grain 06. Another dark rim gave a discordant date of 268 ± 4 Ma, which may reflect common Pb in zircon. Similar Concordia ages of 237.1 ± 4.1 and 236.8 ± 4.7 can be calculated, using the youngest clustered concordant dates (Figure 13d) and excluding the concordant date of the dark rim, respectively. Thus, we interpret this ca. 237 Ma age as the crystallization age of zircons during the emplacement of the Shapa Bay pluton.

The zircon crystals from the weakly deformed Dinahai porphyritic granite (21BCOCS42) are euhedral to elongated, with sharp concentric zoning, suggesting their magmatic origin (Figure 13e). All the grains evolve progressively from CL-bright in their core to CL-dark at their rims. Few grains have inherited cores, which are strongly resorbed (e.g., grain 09 and 10). Similarly to zircons from the Shapa Bay pluton, few crystal cores were partly affected by recrystallization as highlighted by CL-dark featureless area (grains 05, 08) and CL-gray to bright transgressive recrystallization front (grain 03). An analyzed inherited core yielded a concordant $^{206}Pb/^{238}U$ date of 1,559 ± 37 Ma (Figure 13f). The CL-bright to gray concentrically zoned crystals as well as the CL-dark zoned rims gave similar $^{206}Pb/^{238}U$ dates within error, ranging from 239 ± 5 to 247 ± 5 Ma. These dates allow to calculate a Concordia age of 243.8 ± 3.4 Ma (Figure 13g), which is interpreted as the crystallization age of these magmatic zircons and can be approximated as the emplacement age of the pluton.

In the diatexites from the Jiahai Bay, zircon crystals are euhedral, CL-dark to gray, with clear polygonal sector zoning (Figure 13h). Only few grains show inherited cores, which are strongly resorbed (e.g., grain 01). These cores yielded apparent $^{206}Pb/^{238}U$ dates ranging from 431 ± 7 Ma to 935 ± 16 Ma (Figures 13h and 13i). The sector-zoned crystals gave similar $^{206}Pb/^{238}U$ dates within error, ranging from 236 ± 6 to 243 ± 5. The seven concordant dates gave a Concordia age of 239.0 ± 3.7 Ma (Figure 13j), which is interpreted as the crystallization age of the newly formed zircons during regional partial melting.

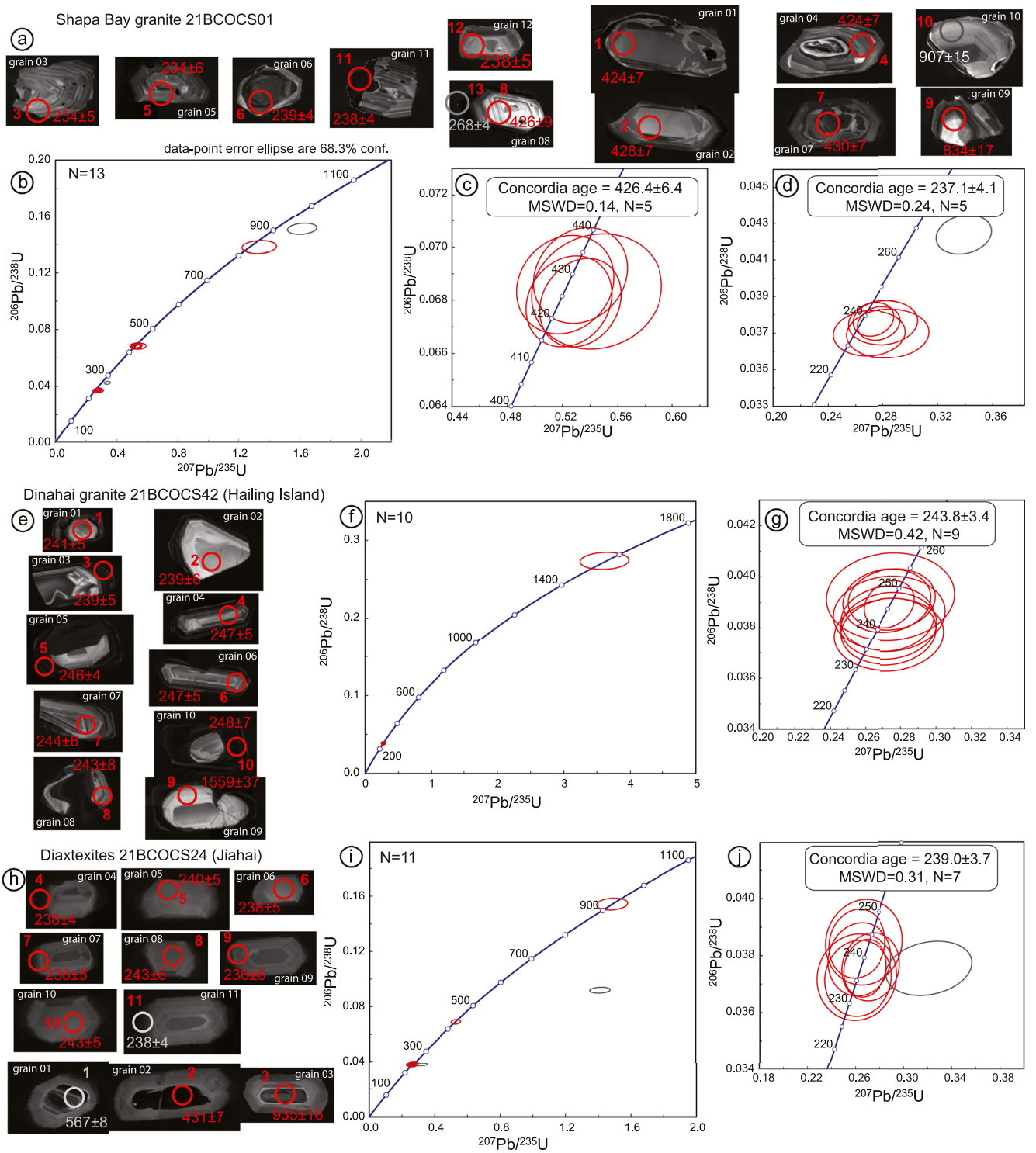

Figure 13. Results of zircons U-Pb dating. (a) Cathodoluminescence images of zircons from the sample 21BCOCS01; (b) Wetherill diagram displaying the analyses made on zircons of the sample 21BCOCS01. (c and d) Zooms of the two main clusters shown in (b). (e) Cathodoluminescence images of zircons from the sample 21BCOCS42; (f) Wetherill diagram displaying the analyses made on zircons of the sample 21BCOCS42 and (g) a zoom of the main cluster; (h) Cathodoluminescence images of the analyzed zircons from the sample 21BCOCS24 with corresponding Wetherill diagram (i) displaying the obtained analyses and a zoom (j) of the main cluster. The red and gray circles on cathodoluminescence images correspond to the spot analysis. On Wetherill diagrams, the red ellipses represent concordant dates and the gray ellipses represent zircon submitted to a lost or a gain in common lead.

5. Discussion

5.1. Age of the Thermal and Deformation Events in the Southern Yunkai Massif and Regional Implications

U-Pb dating reveals one main Concordia age of ca. 240 Ma for the crystallization of plutons and diatexites in the southern Yunkai massif. Our results are similar to those obtained for plutons and migmatites in the studied area, like at Fuhu Hill (Figure 2a). This ca. 240 Ma age also corresponds to the main peak for the crystallization of metamorphic zircons and monazites as well as the latest peak for the crystallization of plutons in the whole Yunkai massif (Figure 2c). Taking into account that magmatism appears as continuous from 265 to 235 Ma, this latest peak at ca. 240 Ma may represent the final crystallization of magma during regional cooling of the partially molten middle-lower crust. It is also suggested by the succession of crystallization ages for zircons (240–235 Ma), monazites (240–230 Ma), and micas (first $^{40}Ar/^{39}Ar$ main peak at 230–225 Ma; Figure 2c). Taking into account the closure temperature of these three geochronometers, such a succession thus reflects the cooling of the gneissic core of the Yunkai massif from ca. 700°C–800°C to 300°C–350°C over 15 my. Thus, the main partial melting event responsible for the emplacement of plutons, migmatites, and the formation of the main ductile fabrics in the southern Yunkai massif cannot be considered as of the Early Paleozoic or Neoproterozoic in age (Z. Chen et al., 2021; J. Zhang et al., 2019). The inherited zircons appear as particularly preserved in weakly molten rocks while syn-kinematic plutons, dykes, and diatexites mostly exhibit Triassic ages (Z. Chen et al., 2021; Y. J. Wang et al., 2021; J. Zhang et al., 2019; this study). It is probably due to inefficient zircon growth in peraluminous protoliths, like Early Paleozoic leucogranites and gneiss, in conditions of low degree of partial melting (see Couzinié et al., 2021 and reference therein). The Yunkai massif was indeed a part of the Early Paleozoic Orogen but its hypothetical inherited structures were erased by the later Permian-Triassic tectono-metamorphic event (e.g., Z. Chen et al., 2017; Y. J. Wang, Fan, Cawood, et al., 2007; Y. J. Wang et al., 2012, this study).

The previous *P-T* estimates of peak metamorphism within the Yunkai massif highlight that melts were produced during the whole Permian-Triassic magmatic event at the same structural level, for pressures ranging between 7 and 5 kbar (Charoy & Barbey, 2008; B. Chen & Zhuang, 1994; K. Zhao, Xu, et al., 2017; H. W. Zhou et al., 1997). U-Pb dating of granulite relicts within plutons suggests that the peak temperature (i.e., 950°C–900°C) was reached at ca. 255–245 Ma (K. Zhao, Xu, et al., 2017; L. Zhao et al., 2010). It implies that melts were continuously produced since 265 Ma and remained mostly trapped at ca. 18–22 km depth until their final crystallization at ca. 240 Ma. Few magmas were extracted up to shallow depth, like the Jiuzhou and Taima granites, which intruded the Late Permian Shiwandashan sedimentary basin, or the Darongshan granite that was emplaced immediately above migmatites (Figure 2a; Charoy & Barbey, 2008). Granulite facies metamorphism and long-lived partial melting at mid-crustal depth imply a persistent high to extremely high geothermal gradient (e.g., Villaros et al., 2018). The accumulation of melt products within a single structural layer triggers gravity instabilities that in turn favor the formation of gneiss domes (e.g., Cochelin et al., 2021; Vanderhaeghe, 2009; Villaros et al., 2018), as highlighted in this study for the southern Yunkai massif (see Section 5.2). Taking into account that migmatites and plutons from the southern Yunkai massif exhibit magmatic fabrics, it implies that the NE-SW crustal flow that characterizes our studied area was active until their crystallization at ca. 240 Ma, and probably since the onset of partial melting under granulite facies in Late Permian times. Strain localization within kilometer-scale retrogressive shear zones at the top of gneiss domes, like in the Hailing Island, also suggests that NE-SW extension may have continued after ca. 240 Ma.

The Permian-Triassic HT metamorphism and associated regional NE-SW extension and gneiss dome formation are in odd with the previous tectonic model by Lin et al. (2008), who interpreted the NE-SW stretching lineations from the basement as the result of Triassic northeastward thrusting. As noticed by Z. Chen et al. (2017), the metamorphic record in the basement suggests that the main ductile fabric was more related to HT metamorphism and extensional tectonics rather than thrust sheets or nappe emplacement (Faure et al., 2016; Lin et al., 2008). Furthermore, nappe emplacement is typical of cold orogens and mechanically incompatible with the persistence of a partially molten middle crust (Brun, 2002; Chardon et al., 2009; Gapais et al., 2009) from 265 to 240 Ma (Figure 2). Furthermore, our microstructural study only highlighted retrogressive deformation, as commonly observed in extensional gneiss domes, while a crustal nappe stacking would normally imply prograde one. Therefore, the geological meaning of the amphibolite facies ductile fabrics within the rest of the Yunkai massif should be reevaluated regarding our new results.

It is worthy to point out that the migmatites were locally reworked by steep shear zones under greenschists facies. Taking into account that the main HT event responsible for the penetrative deformation in the Yunkai massif is of Permian to Triassic in age, the available $^{40}Ar/^{39}Ar$ ages on greenschist facies shear zones from the Yunkai massif (Figure 2) can be reasonably interpreted as the age of the late ductile shearing. Therefore, the late dextral (D2) shear zones can be considered as of Late Triassic in age (i.e., 230–200 Ma, Figure 2c), or even Jurassic in age, as suggested by previous works (Ni et al., 2019, Y. J. Wang et al., 2021; K.-J. Zhang & Cai, 2009). The later (D3) steep dip-slip NNE-SSW shear zones were not dated in the Yunkai massif but may be Jurassic to Cretaceous, like currently observed across South China (e.g., Shu et al., 2009).

5.2. Strain Partitioning Related to Gneiss Dome Formation in the Yunkai Massif

In the studied area, the lower crust recorded at first-order homogeneous deformation (i.e., magmatic orogen-parallel flow) and the accumulation of melt at mid-crustal depth induced the formation of strong rheological contrast close to the fusion front. It led to strain localization into extensional shear zones at the top of the nascent gneiss domes (e.g., Hailing island, Figures 11b and 11c), favoring the exhumation of the high-grade metamorphic rocks in their core. The systematic elongation of gneiss domes parallel to the regional NE-SW direction of stretching suggests that the lower crust was affected by lateral flow in response to the NW-SE horizontal shortening at ca. 265–240 Ma. Indeed, such a configuration (i.e., orogen-parallel stretching and elongation of gneiss domes) is very common in hot orogenic domains still submitted to shortening while collapsing orogens and associated gneiss domes exhibit orogen-normal extension, as exemplified in the Variscan and the Himalayan belts (e.g., Cochelin et al., 2021 and references therein). Nevertheless, some local variations in the dip of the main foliation and the trend and plunge of mineral-stretching lineations suggest a more complex crustal flow at the scale of a single gneiss dome (Figure 14a). In detail, four specific and coeval deformation modes were revealed in the investigated areas by this study, highlighting 3D regional to local-scale strain partitioning: (a) horizontal flow; (b) vertical flow, (c) strike-slip dominated flow, and (d) lateral constrictive flow. These deformation modes are interpreted hereafter as the interplay between tectonics and gravity-driven flow of the partially molten lower crust.

The dominant crustal flow mode described in this study corresponds to the Horizontal Flow, as recorded in Fuhu Hill, the Shapa, and Jiahai bays. At the scale of a gneiss dome, this flow pattern is recorded at the apex of the gneiss dome, that is, the place where foliation planes are horizontal to shallowly dipping (Figure 14a). Crustal flow is mainly parallel to the orogen and associated with opposite senses of shear, with top-to-the south-west and north-east kinematics at the south-western and north-western vicinity of the gneiss dome, respectively. It reflects the lateral escape of the ductile lower crust in response to the regional stress field (i.e., NW-SE horizontal shortening). A local divergence of stretching lineations has been observed within gneiss domes, leading to oblique trends (e.g., Shapa Bay, with WNW-ESE lineations) or almost orogen-normal trends (e.g., Hailing Island). Progressive divergence of stretching lineations at the limbs of gneiss domes is frequently observed within orogen-parallel gneiss domes and reflects gravitational instabilities due to the exhumation of the low buoyant lower crust (Augier et al., 2005; Jolivet et al., 2004; Le Pourhiet et al., 2012; Saspiturry et al., 2019). Within domains having a large portion of melt (i.e., diatexites) and characterized by strong rheological contrasts with the surrounding country-rocks, the gravity-driven flow can induce orogen-normal extension, also called collapse component (e.g., Cochelin et al., 2021; Rutte et al., 2017; Whitney et al., 2004; Worthington et al., 2020; Figure 14a), as recorded locally in the core of the Hailing Island (Figure 11b). Opposite senses of shear at each limb of gneiss domes enhanced the exhumation of deep crustal rocks in the core of domes (see below).

A secondary Vertical Flow mode has been revealed at the zones where melt fraction was high, that is, in diatexites layers and granitic dykes. Such a vertical flow can be observed at all scales, from single channelized leucosome to kilometer-thick diatexite domains showing vertical magmatic fabrics (e.g., western Hailing Island). It reflects the uprising and channeling of melt that are extracted from the deep lower crust (Brown, 1994, 2010; Rosenberg & Berger, 2001; Sawyer, 1998). In our studied area, such vertical extraction is often associated with vertical dykes that cross-cut the horizontal foliation (i.e., horizontal melt segregation; Vigneresse & Tikoff, 1999) of metatexites (Figure 14a). The main pathways for melt ascent are shear bands, as commonly observed in other gneiss domes (e.g., Brown, 1994; Rosenberg & Berger, 2001; Vigneresse & Tikoff, 1999). As described in this study, Vertical Flow and Horizontal Flow can thus occur at the same location and coevally as channeling is mostly controlled, at time t, by the amount of melt and the applied shear stress (Holtzman & Kohlstedt, 2007; Rabinowicz & Vigneresse, 2004; Vigneresse & Burg, 2000). While the leucosomes-scale extraction appears as discontinuous

10.1029/2022TC007457

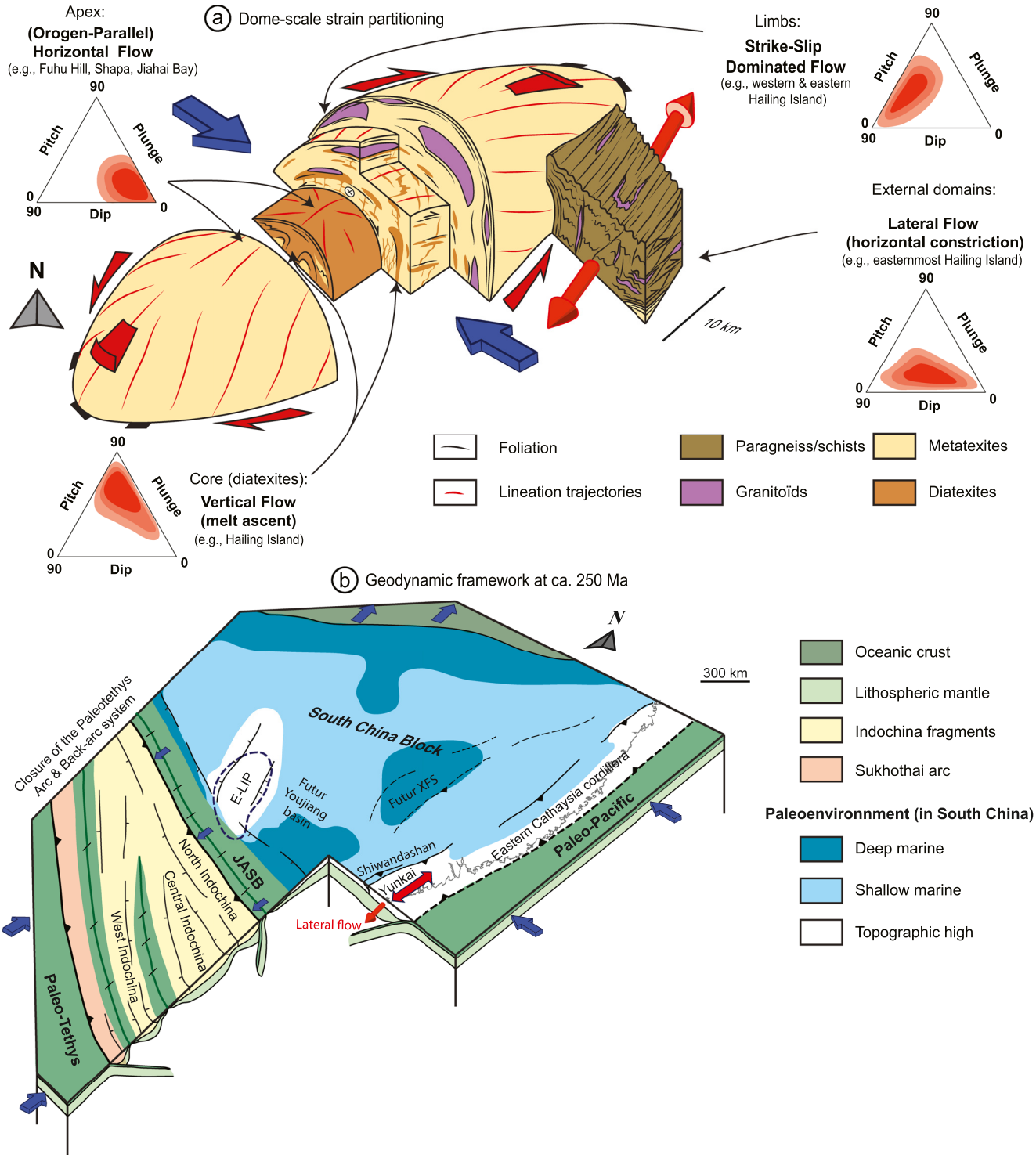

Figure 14. (a) Block-diagrams illustrating strain partitioning processes within the gneiss domes from the Southern Yunkai massif, where lower crustal flow is divided into four end-members (see the text for further explanation). (b) Block-diagram replacing lateral flow deformation mode from the Yunkai massif in a coherent geodynamic context at the Permian-Triassic transition, taking into account the evolution of the Paleo-Tethys realm to the south-west, the Paleo-Pacific to the east and the deformation within the rest of the South China Block (further explanation in the text). Abbreviations: E-LIP, Emeishan Large Igneous Province; JASB, Jinshajiang-Ailaoshan-Song Ma Branch.

during the gneiss dome formation, kilometer-thick channels may reflect continuous melt extraction, feeding the main plutons that intrude the upper part of the dome (Figure 14a) or the upper crust (Vigneresse & Burg, 2000).

With the increasing dip of foliation at the limbs of gneiss domes, the orogen-parallel lineations show a progressive decreasing pitch (Figure 14a). Orogen-parallel horizontal flow evolves progressively into strike-slip dominated flow (e.g., Hailing Island), as frequently observed in non-cylindrical domes (Augier et al., 2005; Cochelin, Gumiaux, et al., 2018; Denèle et al., 2007; Jolivet et al., 2004; Le Pourhiet et al., 2012; Vanderhaeghe, 2004). Like in the core of the gneiss dome, the kinematics from a limb to another are symmetrical and compatible with the main direction of flow in the rest of the dome (Figure 14a). We interpreted the steepening of the extensional fabrics and strike-slip shearing here as the response of the extending crust to the overall NW-SE convergence at ca. 265–240 Ma. It may also be compatible with transcurrent tectonic settings (Le Pourhiet et al., 2012), however, the fact that the strike-slip shear zones mimic the dome shape suggests that their strike and kinematics are rather controlled by the formation of the dome.

The hanging-wall of the shear zones (i.e., the external parts of gneiss domes) was affected by penetrative ductile deformation, which is characterized by L-type structures like weakly defined but strongly folded foliation, folded granitic veins, and pervasive sub-horizontal stretching lineation parallel to the main fold axis. It highlights that the gneissic crust around (i.e., above) the migmatites was affected by penetrative lateral constrictional flow at Early Triassic times (Figure 14a). The main direction of stretching parallelizes the shape of the gneiss domes (Figure 14a). The direction of stretching is thus supposed to be parallel to the orogenic trend but can be oblique close to the termination of gneiss domes, as observed at the Hailing Island (Figure 11b). The kinematics are similar to those observed within the gneiss dome (i.e., extensional to strike-slip) and reflect the regional-scale lateral flow of the hot crust in response to the NW-SE horizontal shortening (Figure 14a).

5.3. Geodynamic Implications of Late Permian-Triassic Lateral Flow in the Yunkai Massif

The NW-SE convergence deduced from this study in the southern Yunkai massif is similar to those described in the rest of Cathaysia and in the Xuefengshan for the Late Permian and the Middle Triassic (Chu, Faure, et al., 2012; Faure et al., 2016; Z.-X. Li & Li, 2007, Figure 1b). During this period, the South China Block was affected by the development of a fold-and-thrust belt, which was propagated to the NW (e.g., Z.-X. Li & Li, 2007) coupled with sparse occurrences of HT metamorphism, scattered plutonism, and volcanism (D. F. Chen et al., 1998; X.-H. Li et al., 2012; Z.-X. Li & Li, 2007; Q. Wang, Li, et al., 2005; D.-S. Yang et al., 2010; L. Zhao, Zhai, et al., 2017). Thus, the SE parts of the South China Block formed a NE-SW active margin since the Late Permian and the Yunkai massif formed its south-westernmost parts (J. Li, Zhao, et al., 2017; X.-H. Li et al., 2012; Z.-X. Li & Li, 2007; Shen et al., 2018; Figure 14b). Such a scheme is supported by paleoenvironment data, showing that at Late Permian times, terrestrial domains were restricted to the main magmatic provinces (i.e., SE Cathaysia and E-LIP, Figure 14b) and the northwestward propagation of the fold-and-thrust belt was responsible to the progressive uplift and final emersion of the shallow to deep marine domains from the western Cathaysia and Xuefengshan during the Lower and Middle Triassic (Y. Wang & Jin, 2000). To the west of the Yunkai massif, the resulting NE-SW-striking retro-arc foreland basins (e.g., the Shiwandashan basin, J. Li, Zhao, et al., 2017; Liang & Li, 2005) were filled with detritus derived from the Late Permian-Early Triassic magmatic rocks that were emplaced in the core of the massif (Hu et al., 2015). Indeed, north-westward thrusting within the retro-arc foreland occurred at least since ca. 253 Ma (J. Li, Zhao, et al., 2017), synchronously with granulite facies metamorphism (i.e., peak metamorphism) at mid-crustal depths and generation of the Darongshan-Shiwandashan magmatic suite (Charoy & Barbey, 2008; J. Li, Zhao, et al., 2017; K. Zhao, Xu, et al., 2017; L. Zhao et al., 2010).

Until now, both the HT metamorphism, magmatism, and the main deformation events in the Yunkai massif were mostly considered as the consequence of the Paleo-Tethys subduction and Indosinian orogeny, at the south-western margin of the South China Block (e.g., Y. Li et al., 2016; Lin et al., 2008; Qing et al., 2020; Qiu et al., 2016; Y. J. Wang et al., 2012, 2021). On the contrary, we propose that partial melting and HT deformation in the Yunkai massif are the consequences of the subduction of the Paleo-Pacific Ocean since the Late Permian, leading to the development of an NE-SW cordillera in SE Cathaysia (Isozaki et al., 2017; Jiao et al., 2015; J. Li, Zhao, et al., 2017; X.-H. Li et al., 2012; Z.-X. Li & Li, 2007; Q. Wang, Li, et al., 2005; X. Zhang et al., 2018; Figure 14b). Indeed, the gneiss dome formation and the associated magmatic event in the Yunkai massif failed to be explained by the collision between South China and Indochina (i.e., the Indosinian orogeny). First of all, the Yunkai massif is located at 400 km to the north-east of the NW-SE-striking Indosinian orogen and immediately

to the east of the main foreland basin of the Indosinian belt (i.e., the Youjiang basin), where turbidites were deposited lately, during the Middle Triassic (Gan et al., 2021). At peak metamorphism within the Yunkai massif (255–245 Ma), the Paleo-Tethys and its back-arc domain were not yet fully consumed and accreted (Figure 14b) as (a) the Indosinian collision started at ca. 245 Ma (e.g., Fan et al., 2015; Liu et al., 2017; R. Y. Zhang et al., 2013), inducing syn to late collisional (245–210 Ma) magmatism within the narrow hinterland (Y. J. Wang et al., 2018 and reference therein) and (b) the south-western margin of the South China Block (i.e., the future Youjiang foreland basin) formed a platform with graben structures (Gan et al., 2021 and references therein), which thus experienced only crustal thinning (e.g., Faure et al., 2014; J. Li, Zhao, et al., 2017; Thanh et al., 2019). Added to these spatially disconnected and diachronous tectono-magmatic events, lateral flow in the Yunkai massif was driven by NW-SE convergence, which is perpendicular to the direction of shortening due to the Indosinian collision (e.g., Faure et al., 2014, 2016; J. Li, Zhang, et al., 2017; J. Li, Zhao, et al., 2017). Thrust sheets and folds associated with the Indosinian convergence were propagated northward into the South China Block only after 245 Ma (J. Li, Zhao, et al., 2017; W.-X. Yang et al., 2021). The only influence of the Indosinian-Cimmerian orogenies in the Yunkai massif is related to this Upper Triassic event, with the activation of the 230–200 Ma greenschist facies dextral shear zones (i.e., D2 in this study, see also Ni et al., 2019; Y. J. Wang, Fan, Cawood, et al., 2007; Y. J. Wang et al., 2021; K.-J. Zhang & Cai, 2009).

Therefore, lateral flow within the mid-lower crust in the Yunkai massif was mainly driven by the subduction of the Paleo-Pacific Ocean at the south-eastern margin of the South China Block (Figure 14b). Eventually, the southwestward subduction of the narrow Jinshajiang-Ailaoshan-Song Ma back-arc sub-branch of the Paleo-Tethys below North Indochina may have favored or amplified the lateral escape of the lower crust southwestward in the Yunkai massif, acting as a supplementary driving force until to the ultimate closure of this secondary oceanic branch (Figure 14b). However, the origin of the HT metamorphism leading to the development of gneiss domes in the Yunkai massif remains unclear and should be further investigated, as it could reflect the consequence of the building cordillera (Z.-X. Li & Li, 2007), or the result of a specific dynamics of the Paleo-Pacific subduction zone and associated crust-mantle interactions (e.g., roll-back; Jiao et al., 2015). Taking into account the similarities between the Yunkai massif and the rest of Cathaysia in terms of (a) deformation patterns and (b) the occurrences of magmatism and HT metamorphism (including granulites), lateral flow at middle to lower-crustal depth may have occurred not only in the Yunkai massif but also elsewhere in the newly formed NE-SW belt (J. Li et al., 2022). Therefore, the formation of a cordillera in the Late-Permian-Middle Triassic suggests that this belt may have experienced a similar tectonic evolution than the Andean orogenic system, with the development of an orogenic plateau, as suggested by Chu et al. (2020). The estimated width (i.e., ca. 800–1,300 km) of this orogenic belt (Z.-X. Li & Li, 2007) is rather similar to the one of the Himalayan-Tibet orogenic system (Vanderhaeghe, 2009), suggesting a widespread and penetrative deformation of the whole Cathaysia sub-block. Such consideration rises fundamental implications on how Permian-Triassic shortening was accommodated within Cathaysia (e.g., localized vs. distributed) and requires further investigations.

6. Conclusions

Our field investigations in the anatectic core of the Yunkai massif highlight that migmatization and the emplacement of the main plutons occurred in a context of NE-SW extension and gneiss dome formation. The exhumation of high-grade rocks within these gneiss domes is characterized by lateral and vertical strain partitioning reflecting the competition between tectonics (i.e., regional NW-SE horizontal shortening) and gravity forces. The overall gneiss domes recorded dominant lateral flow (i.e., tectonic-driven), which is highlighted by (a) horizontal lateral flow at the core and the hinge of gneiss domes, (b) strike-slip dominated flow at the limbs of gneiss domes and, (c) constrictive lateral flow at the external parts of the gneiss domes. Their cores (i.e., where melts are produced) are characterized by significant vertical flow (i.e., gravity-driven flow).

The dated diatexites and plutons yield similar U-Pb ages of ca. 240 Ma, which is interpreted as the crystallization age of these anatectic rocks after their emplacement. The main thermal event responsible for partial melting and high-grade ductile deformation in the Yunkai massif is thus Late Paleozoic to Early Mesozoic in age, reworking the Early Paleozoic orogen and erasing its inherited ductile fabrics.

The HT tectono-metamorphic event in the Yunkai massif appears as disconnected from the Indosinian orogeny but rather related to the Paleo-Pacific subduction at the south-eastern margin of the South China Block. Deep

crustal lateral flow may have been amplified by the ongoing subduction of the JASB secondary branch of the Paleo-Tethys below North Indochina, acting as a plausible additional driving force. The later propagation of the Indosinian front within the South China Block during the Upper Triassic may be responsible for the formation of the late greenschist facies dextral shear zones that cross-cut the gneiss domes in the Yunkai massif. Taking into account that syn-convergence magmatism and HT metamorphism have been demonstrated in other parts of Cathaysia during the Late Permian and Middle Triassic, lateral flow of the deep crust may have been a more common way to balance NW-SE shortening in the South China Block than previously expected.

Data Availability Statement

All data presented in this study are available in the Figures and Supporting Information Files. The structural measurements are provided in Figures 4, 5, 7, 9, and 11 and Figure S1. Zircon geochronology analysis data are available in Table S3. These data are also freely available in the Earthchem Library (https://doi.org/10.26022/IEDA/112517).

Acknowledgments
This study was financially supported by the National Natural Science Foundation of China (Grants 42202230, 42050410312, 42161144013) and the Open Fund of State Key Laboratory for Mineral Deposits Research of Nanjing. The authors thank Y. Pan and D. Xiong from Nanjing University for their technical support during U-Pb dating. M. Faure is acknowledged for fruitful discussion concerning the tectonic evolution of SE Asia and his helpful comments on an early version of the manuscript. The authors acknowledge Y. Chu and an anonymous reviewer for helping to improve the manuscript and S. Li for editorial handling.

References

Augier, R., Jolivet, L., & Robin, C. (2005). Late orogenic doming in the eastern Betic Cordilleras: Final exhumation of the Nevado-Filabride complex and its relation to basin genesis. *Tectonics*, *24*(4), TC4003. https://doi.org/10.1029/2004TC001687

Balé, P., & Brun, J.-P. (1989). Late Precambrian thrust and wrench zones in northern Brittany (France). *Journal of Structural Geology*, *11*(4), 391–405. https://doi.org/10.1016/0191-8141(89)90017-5

Brown, M. (1994). The generation, segregation, ascent, and emplacement of granite magma: The migmatite-to-crustally derived granite connection in thickened orogens. *Earth-Science Reviews*, *36*(1), 83–130. https://doi.org/10.1016/0012-8252(94)90009-4

Brown, M. (2010). Melting of the continental crust during orogenesis: The thermal, rheological, and compositional consequences of melt transport from lower to upper continental crust. *Canadian Journal of Earth Sciences*, *47*(5), 655–694. https://doi.org/10.1139/E09-057

Brun, J.-P. (2002). Deformation of the continental lithosphere: Insights from brittle-ductile models. *Geological Society, London, Special Publications*, *200*, 355–370. https://doi.org/10.1144/gsl.sp.2001.200.01.20.2001.200.01.20

Bureau of Guangdong Geology and Mineral Resources (BGMRGD). (1988). *Regional geology of the Guangdong Province (p. 914)*. Beijing: Geological Publishing House.

Bureau of Guangxi Geology and Mineral Resources (BGMRGX). (1985). *Regional geology of the Guangxi Zhuang autonomous region (p. 853)*. Beijing: Geological Publishing House.

Chardon, D., Gapais, D., & Cagnard, F. (2009). Flow of ultra-hot orogens: A view from the Precambrian, clues for the Phanerozoic. *Tectonophysics*, *477*(3–4), 105–118. https://doi.org/10.1016/j.tecto.2009.03.008

Charoy, B., & Barbey, P. (2008). Ferromagnesian silicate association in S-type granites: The Darongshan granitic complex (Guangxi, South China). *Bulletin de la Societe Geologique de France*, *179*(1), 13–27. https://doi.org/10.2113/gssgfbull.179.1.13

Charvet, J., Shu, L., Faure, M., Choulet, F., Wang, B., Lu, H., & Breton, N. L. (2010). Structural development of the Lower Paleozoic belt of South China: Genesis of an intracontinental orogen. *Journal of Asian Earth Sciences*, *39*(4), 309–330. https://doi.org/10.1016/j.jseaes.2010.03.006

Chen, A. (1999). Mirror-image thrusting in the South China orogenic belt: Tectonic evidence from western Fujian, southeastern China. *Tectonophysics*, *305*(4), 497–519. https://doi.org/10.1016/S0040-1951(99)00036-0

Chen, B., & Zhuang, Y. X. (1994). Petrology and petrogenesis of Yunlu charnockite and its granulite inclusion, west Guangdong, South China. *Acta Petrologica Sinica*, *10*, 139–150.

Chen, C.-H., Hsieh, P.-S., Lee, C.-Y., & Zhou, H.-W. (2011). Two episodes of the Indosinian thermal event on the South China Block: Constraints from LA-ICPMS U-Pb zircon and electron microprobe monazite ages of the Darongshan S-type granitic suite. *Gondwana Research*, *19*(4), 1008–1023. https://doi.org/10.1016/j.gr.2010.10.009

Chen, C.-H., Liu, Y.-H., Lee, C.-Y., Sano, Y., Zhou, H.-W., Xiang, H., & Takahata, N. (2017). The Triassic reworking of the Yunkai massif (South China): EMP monazite and U-Pb zircon geochronologic evidence. *Tectonophysics*, *694*, 1–22. https://doi.org/10.1016/j.tecto.2016.11.022

Chen, D. F., Li, X. H., Pan, J., Dong, W., Chen, G., & Chen, X. (1998). Metamorphic newly produced zircons, SHRIMP iron microprobe U-Pb age of amphibolite of Hexi Group, Zhejiang and its implications. *Acta Mineralogica Sinica*, *18*, 396–400.

Chen, Z., Liu, Y., Jin, W., Lou, F., & Chen, G. (2021). A preliminary study of the siliceous and femic rock blocks in the Neoproterozoic diatexitic granite at Fuhu Hill in southwestern Guangdong, China. *Geological Journal*, *56*(6), 2888–2905. https://doi.org/10.1002/gj.4076

Chu, Y., Faure, M., Lin, W., Wang, Q., & Ji, W. (2012). Tectonics of the Middle Triassic intracontinental Xuefengshan belt, South China: New insights from structural and chronological constraints on the basal décollement zone. *International Journal of Earth Sciences*, *101*(8), 2125–2150. https://doi.org/10.1007/s00531-012-0780-5

Chu, Y., & Lin, W. (2014). Phanerozoic polyorogenic deformation in southern Jiuling Massif, northern South China Block: Constraints from structural analysis and geochronology. *Journal of Asian Earth Sciences*, *86*, 117–130. https://doi.org/10.1016/j.jseaes.2013.05.019

Chu, Y., & Lin, W. (2018). Strain analysis of the Xuefengshan belt, South China: From internal strain variation to formation of the orogenic curvature. *Journal of Structural Geology*, *116*, 131–145. https://doi.org/10.1016/j.jsg.2018.08.002

Chu, Y., Lin, W., Faure, M., Allen, M. B., & Feng, Z. (2020). Cretaceous exhumation of the Triassic intracontinental Xuefengshan belt: Delayed unroofing of an orogenic plateau across the South China Block? *Tectonophysics*, *793*, 228592. https://doi.org/10.1016/j.tecto.2020.228592

Chu, Y., Lin, W., Faure, M., Wang, Q., & Ji, W. (2012). Phanerozoic tectonothermal events of the Xuefengshan belt, central South China: Implications from U-Pb age and Lu-Hf determinations of granites. *Lithos*, *150*, 243–255. https://doi.org/10.1016/j.lithos.2012.04.005

Cochelin, B., Gumiaux, C., Chardon, D., Denèle, Y., & Le Bayon, B. (2018). Multi-scale strainfield analysis using geostatistics: Investigating the rheological behavior of the hot Variscan crust of the Pyrenees (axial zone). *Journal of Structural Geology*, *116*, 114–130. https://doi.org/10.1016/j.jsg.2018.07.024

Cochelin, B., Lemirre, B., Denèle, Y., & de Saint Blanquat, M. (2021). Strain partitioning within bending orogens, new insights from the Variscan belt (Chiroulet-Lesponne Domes, Pyrenees). *Tectonics*, *40*(7), e2020TC006386. https://doi.org/10.1029/2020TC006386

Cochelin, B., Lemirre, B., Denèle, Y., de Saint Blanquat, M., Lahfid, A., & Duchêne, S. (2018). Structural inheritance in the Central Pyrenees: The Variscan to Alpine tectonometamorphic evolution of the axial zone. *Journal of the Geological Society*, *175*, 336–351. https://doi.org/10.1144/jgs2017-066

Couzinié, S., Bouilhol, P., Laurent, O., Marko, L., & Moyen, J.-F. (2021). When zircon drowns: Elusive geochronological record of water-fluxed orthogneiss melting in the Velay dome (Massif Central, France). *Lithos*, *384–385*, 105938. https://doi.org/10.1016/j.lithos.2020.105938

da Silva, L. C., Pedrosa-Soares, A. C., Armstrong, R., Pinto, C. P., Magalhães, J. T. R., Pinheiro, M. A. P., & Santos, G. G. (2016). Disclosing the Paleoarchean to Ediacaran history of the São Francisco craton basement: The Porteirinha domain (northern Araçuaí orogen, Brazil). *Journal of South American Earth Sciences*, *68*, 50–67. https://doi.org/10.1016/j.jsames.2015.12.002

Denèle, Y., Olivier, P., Gleizes, G., & Barbey, P. (2007). The Hospitalet gneiss dome (Pyrenees) revisited: Lateral flow during Variscan transpression in the middle crust. Terra Nova. *Terra Nova*, *19*(6), 445–453. https://doi.org/10.1111/j.1365-3121.2007.00770.x

Dodson, M. H. (1973). Closure temperature in cooling geochronological and petrological systems. *Contributions to Mineralogy and Petrology*, *40*(3), 259–274. https://doi.org/10.1007/BF00373790

Fan, W., Wang, Y., Zhang, Y., Zhang, Y., Jourdan, F., Zi, J., & Liu, H. (2015). Paleotethyan subduction process revealed from Triassic blueschists in the Lancang tectonic belt of Southwest China. *Tectonophysics*, *662*, 95–108. https://doi.org/10.1016/j.tecto.2014.12.021

Faure, M., Lepvrier, C., Nguyen, V. V., Vu, T. V., Lin, W., & Chen, Z. (2014). The South China Block-Indochina collision: Where, when, and how? *Journal of Asian Earth Sciences*, *79*, 260–274. https://doi.org/10.1016/j.jseaes.2013.09.022

Faure, M., Lin, W., Chu, Y., & Lepvrier, C. (2016). Triassic tectonics of the southern margin of the South China Block. *Comptes Rendus Geoscience*, *348*(1), 5–14. https://doi.org/10.1016/j.crte.2015.06.012

Faure, M., Nguyen, V. V., Hoai, L. T. T., & Leprier, C. (2018). Early Paleozoic or Early-Middle Triassic collision between the South China and Indochina Blocks: The controversy resolved? Structural insights from the Kon Tum massif (Central Vietnam). *Journal of Asian Sciences*, *166*, 162–180. https://doi.org/10.1016/j.jseaes.2018.07.015

Faure, M., Shu, L., Wang, B., Charvet, J., Choulet, F., & Monie, P. (2009). Intracontinental subduction: A possible mechanism for the Early Palaeozoic orogen of SE China. *Terra Nova*, *21*(5), 360–368. https://doi.org/10.1111/j.1365-3121.2009.00888.x

Fossen, H., & Cavalcante, G. C. G. (2017). Shear zones—A review. *Earth-Science Reviews*, *171*, 434–455. https://doi.org/10.1016/j.earscirev.2017.05.002

Gan, C., Wang, Y., Zhang, Y., Qian, X., & Zhang, A. (2021). The assembly of the South China and Indochina Blocks: Constraints from the Triassic felsic volcanics in the Youjiang basin. *GSA Bulletin*, *133*(9–10), 2097–2112. https://doi.org/10.1130/B35816.1

Gao, P., Zheng, Y.-F., & Zhao, Z.-F. (2017). Triassic granites in South China: A geochemical perspective on their characteristics, petrogenesis, and tectonic significance. *Earth-Science Reviews*, *173*, 266–294. https://doi.org/10.1016/j.earscirev.2017.07.016

Gapais, D. (1987). *Les orthogneiss: Structures, mécanismes de déformation et analyse cinématique, (Ph.D. thesis)*. France: University of Rennes 1.

Gapais, D. (1989). Shear structures within deformed granites: Mechanical and thermal indicators. *Geology*, *17*(12), 1144–1147. https://doi.org/10.1130/0091-7613(1989)017<1144:SSWDGM>2.3.CO;2

Gapais, D., Cagnard, F., Gueydan, F., Barbey, P., & Ballèvre, M. (2009). Mountain building and exhumation processes through time: Inferences from nature and models. *Terra Nova*, *21*(3), 188–194. https://doi.org/10.1111/j.1365-3121.2009.00873.x

Guo, L., Shi, Y., Lu, H., Ma, R., Dong, H., & Yang, S. (1989). The pre-Devonian tectonic patterns and evolution of South China. *Journal of Southeast Asian Earth Sciences*, *3*(1), 87–93. https://doi.org/10.1016/0743-9547(89)90012-3

Hacker, B. R., Ratschbacher, L., & Liou, J. G. (2004). Subduction, collision, and exhumation in the ultrahigh-pressure Qinling-Dabie orogen. *Geological Society, London, Special Publications*, *226*, 157–175. https://doi.org/10.1144/GSL.SP.2004.226.01.09

Harrison, T. M., Duncan, I., & McDougall, I. (1985). Diffusion of ^{40}Ar in biotite: Temperature, pressure and compositional effects. *Geochimica et Cosmochimica Acta*, *49*(11), 2461–2468. https://doi.org/10.1016/0016-7037(85)90246-7

Hieu, P. T., Anh, N. T. Q., Minh, P., & Thuy, N. T. B. (2020). Geochemistry, zircon U-Pb ages and Hf isotopes of the Muong Luan granitoid pluton, Northwest Vietnam and its petrogenetic significance. *Island Arc*, *29*(1), e12330. https://doi.org/10.1111/iar.12330

Hirth, G., & Tullis, J. (1992). Dislocation creep regimes in quartz aggregates. *Journal of Structural Geology*, *14*(2), 145–159. https://doi.org/10.1016/0191-8141(92)90053-Y

Holtzman, B. K., & Kohlstedt, D. L. (2007). Stress-driven melt segregation and strain partitioning in partially molten rocks: Effects of stress and strain. *Journal of Petrology*, *48*(12), 2379–2406. https://doi.org/10.1093/petrology/egm065

Hu, L., Cawood, P. A., Du, Y., Xu, Y., Xu, W., & Huang, H. (2015). Detrital records for Upper Permian-Lower Triassic succession in the Shiwandashan basin, South China and implication for Permo-Triassic (Indosinian) orogeny. *Journal of Asian Earth Sciences*, *98*, 152–166. https://doi.org/10.1016/j.jseaes.2014.11.007

Isozaki, Y., Nakahata, H., Zakharov, Y. D., Popov, A. M., Sakata, S., & Hirata, T. (2017). Greater South China extended to the Khanka Block: Detrital zircon geochronology of middle-upper Paleozoic sandstones in Primorye, far East Russia. *Journal of Asian Earth Sciences*, *145*, 565–575. https://doi.org/10.1016/j.jseaes.2017.06.027

Jiao, S.-J., Li, X.-H., Huang, H.-Q., & Deng, X.-G. (2015). Metasedimentary melting in the formation of charnockite: Petrological and zircon U-Pb-Hf-O isotope evidence from the Darongshan S-type granitic complex in southern China. *Lithos*, *239*, 217–233. https://doi.org/10.1016/j.lithos.2015.10.004

Jolivet, L., Famin, V., Mehl, C., Parra, T., Aubourg, C., Hébert, R., & Philippot, P. (2004). Strain localization during crustal-scale boudinage to form extensional metamorphic domes in the Aegean Sea. *Geological Society of America Special Paper*, *380*, 185. https://doi.org/10.1130/0-8137-2380-9.185

Le Pourhiet, L., Huet, B., May, D. A., Labrousse, L., & Jolivet, L. (2012). Kinematic interpretation of the 3D shapes of metamorphic core complexes. *Geochemistry, Geophysics, Geosystems*, *13*(9). https://doi.org/10.1029/2012gc004271

Li, J., Zhang, Y., Ratschbacher, L., Zhao, G., Dong, S., Xin, Y., & Lü, F. (2022). Polyphase deformation in the Badu complex: Insights into Triassic intraplate orogeny in South China. *Journal of Structural Geology*, *154*, 104475. https://doi.org/10.1016/j.jsg.2021.104475

Li, J., Zhang, Y., Zhao, G., Johnston, S. T., Dong, S., Koppers, A., et al. (2017). New insights into Phanerozoic tectonics of South China: Early Paleozoic sinistral and Triassic dextral transpression in the east Wuyishan and Chencai domains, NE Cathaysia. *Tectonics*, *36*(5), 819–853. https://doi.org/10.1002/2016TC004461

Li, J., Zhao, G., Johnston, S. T., Dong, S., Zhang, Y., Xin, Y., et al.(2017). Permo-Triassic structural evolution of the Shiwandashan and Youjiang structural belts, South China. *Journal of Structural Geology*, *100*, 24–44. https://doi.org/10.1016/j.jsg.2017.05.004

Li, X.-H., Li, W.-X., Li, Z.-X., Lo, C.-H., Wang, J., Ye, M.-F., & Yang, Y.-H. (2009). Amalgamation between the Yangtze and Cathaysia Blocks in South China: Constraints from SHRIMP U-Pb zircon ages, geochemistry, and Nd-Hf isotopes of the Shuangxiwu volcanic rocks. *Precambrian Research*, *174*(1), 117–128. https://doi.org/10.1016/j.precamres.2009.07.004

Li, X.-H., Li, Z.-X., He, B., Li, W.-X., Li, Q.-L., Gao, Y., & Wang, X.-C. (2012). The Early Permian active continental margin and crustal growth of the Cathaysia Block: In situ U-Pb, Lu-Hf, and O isotope analyses of detrital zircons. *Chemical Geology*, *328*, 195–207. https://doi.org/10.1016/j.chemgeo.2011.10.027

Li, Y., Wei, J., Santosh, M., Tan, J., Fu, L., & Zhao, S. (2016). Geochronology and petrogenesis of Middle Permian S-type granitoid in southeastern Guangxi Province, South China: Implications for closure of the eastern Paleo-Tethys. *Tectonophysics*, *682*, 1–16. https://doi.org/10.1016/j.tecto.2016.05.048

Li, Z. X., Bogdanova, S. V., Collins, A. S., Davidson, A., De Waele, B., Ernst, R. E., et al. (2008). Assembly, configuration, and break-up history of Rodinia: A synthesis. *Precambrian Research*, *160*(1), 179–210. https://doi.org/10.1016/j.precamres.2007.04.021

Li, Z.-X., & Li, X.-H. (2007). Formation of the 1,300 km wide intracontinental orogen and postorogenic magmatic province in Mesozoic South China: A flat-slab subduction model. *Geology*, *35*(2), 179–182. https://doi.org/10.1130/G23193A.1

Liang, X., & Li, X. (2005). Late Permian to Middle Triassic sedimentary records in Shiwandashan basin: Implication for the Indosinian Yunkai Orogenic Belt, South China. *Sedimentary Geology*, *177*(3), 297–320. https://doi.org/10.1016/j.sedgeo.2005.03.009

Lin, W., Faure, M., Sun, Y., Shu, L., & Wang, Q. (2001). Compression to extension switch during the Middle Triassic orogeny of Eastern China: The case study of the Jiulingshan massif in the southern foreland of the Dabieshan. *Journal of Asian Earth Sciences*, *20*(1), 31–43. https://doi.org/10.1016/S1367-9120(01)00020-7

Lin, W., Wang, Q., & Chen, K. (2008). Phanerozoic tectonics of South China Block: New insights from the polyphase deformation in the Yunkai massif. *Tectonics*, *27*(6). https://doi.org/10.1029/2007TC002207

Liu, H., Peng, T., & Guo, X. (2018). Geochronological and geochemical constraints on the coexistent N-MORB- and SSZ-type ophiolites in Babu area (SW China) and tectonic implications. *Journal of the Geological Society*, *175*(4), 667–678. https://doi.org/10.1144/jgs2017-121

Liu, H., Wang, Y., & Zi, J.-W. (2017). Petrogenesis of the Dalongkai ultramafic-mafic intrusion and its tectonic implication for the Paleotethyan evolution along the Ailaoshan tectonic zone (SW China). *Journal of Asian Earth Sciences*, *141*, 112–124. https://doi.org/10.1016/j.jseaes.2016.07.015

Ludwig, K. R. (2003). User's manual for isoplot 3.00: A geochronlogical toolkit for Microsoft excel. *Berkeley Geochronology Center Special Publication*, *4*, 25–32.

Menegon, L., Pennacchioni, G., & Stünitz, H. (2006). Nucleation and growth of myrmekite during ductile shear deformation in metagranites. *Journal of Metamorphic Geology*, *24*(7), 553–568. https://doi.org/10.1111/j.1525-1314.2006.00654.x

Ni, J., Liu, J., Wang, J., Tang, X., Wang, Z., Li, Z., & Li, D. (2019). Ductile shear deformation and gold mineralization in the Hetai goldfield of the Yunkai massif, South China Block. *Geological Journal*, *54*(2), 929–945. https://doi.org/10.1002/gj.3430

Nosenzo, F., Manzotti, P., Poujol, M., Ballèvre, M., & Langlade, J. (2022). A window into an older orogenic cycle: *P-T* conditions and timing of the pre-Alpine history of the Dora-Maira Massif (Western Alps). *Journal of Metamorphic Geology*, *40*(4), 789–821. https://doi.org/10.1111/jmg.12646

Qing, L., Jiang, Y.-H., & Du, F.-G. (2020). Geodynamics of Late Paleozoic to Early Mesozoic magmatism in South China: Insights from the Genesis of the Late Permian S-type granites in the Yunkai massif. *The Journal of Geology*, *128*(3), 275–301. https://doi.org/10.1086/708465

Qiu, X.-F., Yang, H.-M., Zhao, X.-M., Lu, S.-S., Wu, N.-W., Zhang, L.-G., & Zhang, C.-H. (2016). Early Triassic gneissoid granites in the Gaozhou Area (Yunkai massif), South China: Implications for the amalgamation of the Indochina and South China Blocks. *The Journal of Geology*, *124*(3), 395–409. https://doi.org/10.1086/685765

Rabinowicz, M., & Vigneresse, J.-L. (2004). *Melt segregation under compaction and shear channeling: Application to granitic magma segregation in a continental crust*. Journal of Geophysical Research: Solid Earth, *109*(B4). https://doi.org/10.1029/2002JB002372

Ramsay, J. G. (1967). *Folding and fracturing of rocks (McGraw-Hill)*. New York.

Rosenberg, C. L., & Berger, A. (2001). Syntectonic melt pathways in granitic gneisses, and melt-induced transitions in deformation mechanisms. *Physics and Chemistry of the Earth—Part A: Solid Earth and Geodesy*, *26*(4), 287–293. https://doi.org/10.1016/S1464-1895(01)00058-8

Rutte, D., Ratschbacher, L., Khan, J., Stübner, K., Hacker, B. R., Stearns, M. A., et al. (2017). Building the Pamir-Tibet Plateau—Crustal stacking, extensional collapse, and lateral extrusion in the Central Pamir: 2. Timing and rates. *Tectonics*, 2016TC004294. https://doi.org/10.1002/2016TC004294

Saspiturry, N., Cochelin, B., Razin, P., Leleu, S., Lemirre, B., Bouscary, C., et al. (2019). Tectono-sedimentary evolution of a rift system controlled by Permian post-orogenic extension and metamorphic core complex formation (Bidarray basin and Ursuya dome, Western Pyrenees). *Tectonophysics*, *768*, 228180. https://doi.org/10.1016/j.tecto.2019.228180

Sawyer, E. W. (1998). Formation and evolution of granite magmas during crustal reworking: The significance of diatexites. *Journal of Petrology*, *39*(6), 1147–1167. https://doi.org/10.1093/petroj/39.6.1147

Shellnutt, J. G. (2014). The Emeishan large igneous province: A synthesis. *Geoscience Frontiers*, *5*(3), 369–394. https://doi.org/10.1016/j.gsf.2013.07.003

Shen, L., Yu, J.-H., O'Reilly, S. Y., & Griffin, W. L. (2018). Tectonic switching of southeast China in the Late Paleozoic. *Journal of Geophysical Research: Solid Earth*, *123*(10), 8508–8526. https://doi.org/10.1029/2018JB015520

Shu, L., Wang, B., Cawood, P. A., Santosh, M., & Xu, Z. (2015). Early Paleozoic and Early Mesozoic intraplate tectonic and magmatic events in the Cathaysia Block, South China. *Tectonics*, *34*(8), 1600–1621. https://doi.org/10.1002/2015TC003835

Shu, L., Wang, J., & Yao, J. (2019). Tectonic evolution of the eastern Jiangnan region, South China: New findings and implications on the assembly of the Rodinia supercontinent. *Precambrian Research*, *322*, 42–65. https://doi.org/10.1016/j.precamres.2018.12.007

Shu, L., Yao, J., Wang, B., Faure, M., Charvet, J., & Chen, Y. (2021). Neoproterozoic plate tectonic process and Phanerozoic geodynamic evolution of the South China Block. *Earth-Science Reviews*, *216*, 103596. https://doi.org/10.1016/j.earscirev.2021.103596

Shu, L., Zhou, X. M., Deng, P., Wang, B., Jiang, S. Y., Yu, J. H., & Zhao, X. X. (2009). Mesozoic tectonic evolution of the Southeast China Block: New insights from basin analysis. *Journal of Asian Earth Sciences*, *34*(3), 376–391. https://doi.org/10.1016/j.jseaes.2008.06.004

Song, M., Shu, L., & Santosh, M. (2017). Early Mesozoic intracontinental orogeny and stress transmission in South China: Evidence from Triassic peraluminous granites. *Journal of the Geological Society*, *174*(3), 591–607. https://doi.org/10.1144/jgs2016-098

Stipp, M., Stünitz, H., Heilbronner, R., & Schmid, S. M. (2002). The eastern Tonale fault zone: A "natural laboratory" for crystal plastic deformation of quartz over a temperature range from 250°C to 700°C. *Journal of Structural Geology*, *24*(12), 1861–1884. https://doi.org/10.1016/S0191-8141(02)00035-4

Thanh, T. V., Hieu, P. T., Minh, P., Nhuan, D. V., & Thuy, N. T. B. (2019). Late Permian-Triassic granitic rocks of Vietnam: The Muong Lat example. *International Geology Review*, *61*(15), 1823–1841. https://doi.org/10.1080/00206814.2018.1561335

Vanderhaeghe, O. (2004). Structural development of the Naxos migmatite dome. https://doi.org/10.1130/0-8137-2380-9.211

Vanderhaeghe, O. (2009). Migmatites, granites, and orogeny: Flow modes of partially molten rocks and magmas associated with melt/solid segregation in orogenic belts. *Tectonophysics*, *477*(3–4), 119–134. https://doi.org/10.1016/j.tecto.2009.06.021

Vigneresse, J. L., & Burg, J. p. (2000). Continuous vs. discontinuous melt segregation in migmatites: Insights from a cellular automaton model. *Terra Nova*, *12*(4), 188–192. https://doi.org/10.1046/j.1365-3121.2000.00299.x

Vigneresse, J. L., & Tikoff, B. (1999). Strain partitioning during partial melting and crystallizing felsic magmas. *Tectonophysics*, *312*(2), 117–132. https://doi.org/10.1016/S0040-1951(99)00167-5

Villaros, A., Laurent, O., Couzinié, S., Moyen, J.-F., & Mintrone, M. (2018). Plutons and domes: The consequences of anatectic magma extraction—Example from the southeastern French Massif Central. *International Journal of Earth Sciences*, *107*(8), 2819–2842. https://doi.org/10.1007/s00531-018-1630-x

Wang, B., Shu, L. S., Faure, M., Jahn, B. M., Lo, C. H., Charvet, J., & Liu, H. S. (2014). Phanerozoic multistage tectonic rejuvenation of the continental crust of the Cathaysia Block: Insights from structural investigations and combined zircon U-Pb and Mica $^{40}Ar/^{39}Ar$ geochronology of the granitoids in Southern Jiangxi Province. *The Journal of Geology*, *122*(3), 309–328. https://doi.org/10.1086/675664

Wang, D., Zheng, J., Ma, Q., Griffin, W. L., Zhao, H., & Wong, J. (2013). Early Paleozoic crustal anatexis in the intraplate Wuyi-Yunkai orogen, South China. *Lithos*, *175–176*, 124–145. https://doi.org/10.1016/j.lithos.2013.04.024

Wang, D. Z., Shu, L. S., Faure, M., & Sheng, W. Z. (2001). Mesozoic magmatism and granitic dome in the Wugongshan Massif, Jiangxi Province and their genetical relationship to the tectonic events in southeast China. *Tectonophysics*, *339*(3), 259–277. https://doi.org/10.1016/S0040-1951(01)00130-5

Wang, J., Wang, Z., Geng, W., Yin, Y., & Yang, M. (1994). The discovery of the detachement fault at west of Yunkai uplifting and its tectonic significance. *Chinese Science Bulletin*, *39*, 1886–1888.

Wang, J.-Q., Shu, L.-S., & Yu, J.-H. (2017). From the Neoproterozoic mafic rock to the Silurian high-grade metamorphic rock: Evidence from zircon U-Pb geochronological, bulk-rock geochemical and mineral EPMA studies of Longyou garnet amphibolite in SE China. *Journal of Asian Earth Sciences*, *141*, 7–23. https://doi.org/10.1016/j.jseaes.2016.11.030

Wang, Q., Li, J.-W., Jian, P., Zhao, Z.-H., Xiong, X.-L., Bao, Z.-W., et al. (2005). Alkaline syenites in eastern Cathaysia (South China): Link to Permian-Triassic transtension. *Earth and Planetary Science Letters*, *230*(3), 339–354. https://doi.org/10.1016/j.epsl.2004.11.023

Wang, X., Xu, D., Wang, L., Zhou, D., Hu, J., & Ke, X. (2020). Reworking of Indosinian tectono-thermal events in the Yunkai massif: Gneissic multi-mineral U-Pb geochronological evidence. *Earth Science*, *45*(5). https://doi.org/10.3799/dqkx.2019.151

Wang, Y., & Jin, Y. (2000). Permian palaeogeographic evolution of the Jiangnan basin, South China. *Paleogeography, Paleoclimatology, Paleoecology*, *160*(1), 35–44. https://doi.org/10.1016/S0031-0182(00)00043-2

Wang, Y. J., Fan, W., Cawood, P. A., Ji, S., Peng, T., & Chen, X. (2007). Indosinian high-strain deformation for the Yunkaidashan tectonic belt, South China: Kinematics and $^{40}Ar/^{39}Ar$ geochronological constraints. *Tectonics*, *26*(6). https://doi.org/10.1029/2007TC002099

Wang, Y. J., Fan, W., Zhao, G., Ji, S., & Peng, T. (2007). Zircon U-Pb geochronology of gneissic rocks in the Yunkai massif and its implications on the Caledonian event in the South China Block. *Gondwana Research*, *12*(4), 404–416. https://doi.org/10.1016/j.gr.2006.10.003

Wang, Y. J., Qian, X., Cawood, P. A., Liu, H., Feng, Q., Zhao, G., et al. (2018). Closure of the East Paleotethyan Ocean and amalgamation of the Eastern Cimmerian and Southeast Asia continental fragments. *Earth-Science Reviews*, *186*, 195–230. https://doi.org/10.1016/j.earscirev.2017.09.013

Wang, Y. J., Wang, Y., Zhang, Y., Cawood, P. A., Qian, X., Gan, C., et al. (2021). Triassic two-stage intra-continental orogenesis of the South China Block, driven by Paleotethyan closure and interactions with adjoining blocks. *Journal of Asian Earth Sciences*, *206*, 104648. https://doi.org/10.1016/j.jseaes.2020.104648

Wang, Y. J., Wu, C., Zhang, A., Fan, W., Zhang, Y., Zhang, Y., et al. (2012). Kwangsian and Indosinian reworking of the eastern South China Block: Constraints on zircon U-Pb geochronology and metamorphism of amphibolites and granulites. *Lithos*, *150*, 227–242. https://doi.org/10.1016/j.lithos.2012.04.022

Wang, Y. J., Zhang, Y., Fan, W., & Peng, T. (2005). Structural signatures and $^{40}Ar/^{39}Ar$ geochronology of the Indosinian Xuefengshan tectonic belt, South China Block. *Journal of Structural Geology*, *27*(6), 985–998. https://doi.org/10.1016/j.jsg.2005.04.004

Whitney, D. L., Teyssier, C., & Vanderhaeghe, O. (2004). Gneiss domes and crustal flow. *Geological Society of America Special Papers*, *380*, 15–33. https://doi.org/10.1130/0-8137-2380-9.15

Worthington, J. R., Ratschbacher, L., Stübner, K., Khan, J., Malz, N., Schneider, S., et al. (2020). The Alichur dome, South Pamir, Western India-Asia collisional zone: Detailing the Neogene Shakhdara-Alichur syn-collisional gneiss-dome complex and connection to lithospheric processes. *Tectonics*, *39*(1), e2019TC005735. https://doi.org/10.1029/2019TC005735

Xiang, H., Zhang, L., Zhou, H., Zhong, Z., Zeng, W., Liu, R., & Jin, S. (2008). U-Pb zircon geochronology and Hf isotope study of metamorphosed basic-ultrabasic rocks from metamorphic basement in southwestern Zhejiang: The response of the Cathaysia Block to Indosinian orogenic event. *Science in China Series D: Earth Sciences*, *51*(6), 788. https://doi.org/10.1007/s11430-008-0053-0

Xu, X. B., Zhang, Y. Q., Shu, L. S., & Jia, D. (2011). La-ICP-MS U-Pb and $^{40}Ar/^{39}Ar$ geochronology of the sheared metamorphic rocks in the Wuyishan: Constraints on the timing of Early Paleozoic and Early Mesozoic tectono-thermal events in SE China. *Tectonophysics*, *501*, 71–86. https://doi.org/10.1016/j.tecto.2011.01.014

Yang, D.-S., Li, X.-H., Li, W.-X., Liang, X.-Q., Long, W.-G., & Xiong, X.-L. (2010). U-Pb and ^{40}Ar-^{39}Ar geochronology of the Baiyunshan gneiss (central Guangdong, South China): Constraints on the timing of early Palaeozoic and Mesozoic tectonothermal events in the Wuyun (Wuyi-Yunkai) orogen. *Geological Magazine*, *147*(4), 481–496. https://doi.org/10.1017/S0016756809990811

Yang, W.-X., Yan, D.-P., Qiu, L., Wells, M. L., Dong, J.-M., Gao, T., et al. (2021). Formation and forward propagation of the Indosinian foreland fold-thrust belt and Nanpanjiang foreland basin in SW China. *Tectonics*, *40*(4), e2020TC006552. https://doi.org/10.1029/2020TC006552

Zhang, J., Liu, W., Yakymchuk, C., Sa, R., Zeng, Z., Ding, R., et al. (2019). Partial melting and crustal deformation during the Early Paleozoic Wuyi-Yunkai orogeny: Insights from zircon U-Pb geochronology and structural analysis of the fuhuling migmatites in the Yunkai Region, South China. *Minerals*, *9*(10), 621. https://doi.org/10.3390/min9100621

Zhang, K.-J., & Cai, J.-X. (2009). NE-SW-trending Hepu-Hetai dextral shear zone in southern China: Penetration of the Yunkai Promontory of South China into Indochina. *Journal of Structural Geology*, *31*(7), 737–748. https://doi.org/10.1016/j.jsg.2009.04.012

Zhang, R. Y., Lo, C.-H., Chung, S.-L., Grove, M., Omori, S., Iizuka, Y., et al. (2013). Origin and tectonic implication of ophiolite and eclogite in the Song Ma Suture Zone between the South China and Indochina Blocks. *Journal of Metamorphic Geology*, *31*(1), 49–62. https://doi.org/10.1111/jmg.12012

Zhang, R. Y., Lo, C.-H., Li, X.-H., Chung, S.-L., Anh, T. T., & Tri, T. V. (2014). U-Pb dating and tectonic implication of ophiolite and metabasite from the Song Ma suture zone, northern Vietnam. *American Journal of Science*, *314*(2), 649–678. https://doi.org/10.2475/02.2014.07

Zhang, X., Takeuchi, M., Ohkawa, M., & Matsuzawa, N. (2018). Provenance of a Permian accretionary complex (Nishiki Group) of the Akiyoshi Belt in Southwest Japan and Paleogeographic implications. *Journal of Asian Earth Sciences*, *167*, 130–138. https://doi.org/10.1016/j.jseaes.2018.01.005

Zhao, K., Xu, X., Erdmann, S., Liu, L., & Xia, Y. (2017). Rapid migration of a magma source from mid-to deep-crustal levels: Insights from restitic granulite enclaves and anatectic granite. *GSA Bulletin*, *129*(11–12), 1708–1725. https://doi.org/10.1130/B31462.1

Zhao, L., Guo, F., Fan, W., Li, C., Qin, X., & Li, H. (2010). Crustal evolution of the Shiwandashan area in South China: Zircon U-Pb-Hf isotopic records from granulite enclaves in Indo-Sinian granites. *Chinese Science Bulletin*, *55*(19), 2028–2038. https://doi.org/10.1007/s11434-010-3225-1

Zhao, L., Zhai, M., Santosh, M., & Zhou, X. (2017). Early Mesozoic retrograded eclogite and mafic granulite from the Badu complex of the Cathaysia Block, South China: Petrology and tectonic implications. *Gondwana Research*, *42*, 84–103. https://doi.org/10.1016/j.gr.2016.10.002

Zhao, L., Zhou, X., Zhai, M., Santosh, M., & Geng, Y. (2015). Zircon U-Th-Pb-Hf isotopes of the basement rocks in northeastern Cathaysia Block, South China: Implications for Phanerozoic multiple metamorphic reworking of a Paleoproterozoic terrane. *Gondwana Research*, *28*, 246–261. https://doi.org/10.1016/j.gr.2014.03.019

Zhong, Z., You, Z., Zhou, H., & Han, Y. (1996). The evolution and basic structural framework of the basement of the Yunkai uplift. *Regional Geology of China*, *15*, 36–43.

Zhou, H. W., You, Z. D., Zhong, Z. Q., & Han, Y. Q. (1997). *Origin of thermal center type of migmatites in the Yunkai uplift* (Vol. 22, pp. 332–338). Earth Science-Journal of China University of Geosciences.

Zhou, X., Zheng, C., Zhou, X., Liang, C., Yang, Y., Sun, X., et al. (2022). Petrology, phase equilibria modeling and zircon U-Pb geochronology of charnockites from the Badu Complex in southwestern Zhejiang: Implications for Indosinian orogenic event of the Cathaysia Block, South China. *Precambrian Research*, *375*, 106679. https://doi.org/10.1016/j.precamres.2022.106679